# Eddy activity in the Arctic Ocean projected to surge in a warming world

Xinyue Li [1], Qiang Wang [1] ✉, Sergey Danilov [1,2], Nikolay Koldunov [1], Caili Liu[1], Vasco Müller[1], Dmitry Sidorenko[1] & Thomas Jung [1,3]

Ocean eddies play a critical role in climate and marine life. In the rapidly warming Arctic, little is known about how ocean eddy activity will change because existing climate models cannot resolve Arctic Ocean mesoscale eddies. Here, by employing a next-generation global sea ice–ocean model with kilometre-scale horizontal resolution in the Arctic, we find a surge of eddy kinetic energy in the upper Arctic Ocean, tripling on average in a four-degree-warmer world. The driving mechanism behind this surge is an increase in eddy generation due to enhanced baroclinic instability. Despite the decline of sea ice, eddy killing (a process in which eddies are dampened by sea ice and winds) will not weaken in its annual mean effect in the considered warming scenario. Our study suggests the importance of adequately representing Arctic eddy activity in climate models for understanding the impacts of its increase on climate and ecosystems.

Mesoscale eddies are ubiquitous small-scale swirling motions in the world ocean[1]—sometimes called the weather of the ocean. Despite their small size, ocean eddies are crucial for transporting heat, salt, carbon, oxygen and nutrients in the ocean and regulating air–sea feedbacks, which in turn have a substantial impact on the Earth's climate and ecosystems[2–8]. Satellite altimetry records reveal that ocean eddy activity increased by 2–5% per decade in eddy-rich regions of the world ocean from 1993 to 2020[9]. High-resolution climate model simulations project that ocean surface eddy kinetic energy (EKE) will continue to intensify in most of the eddy-rich regions in response to future warming, except for the North Atlantic[10]. However, existing knowledge of possible future changes in ocean eddy activity in the Arctic, the region undergoing some of the most dramatic climate change, is very limited partly due to the difficulty in simulating Arctic Ocean mesoscale eddies with a typical size of about ten kilometres or smaller[11–15]. Resolving these eddies requires kilometre-scale resolutions, which are far beyond the capability of the Coupled Model Intercomparison Project (CMIP6) models that were used to inform the last IPCC Assessment Report. Moreover, available observations of Arctic eddies are severely limited due to the remoteness, harshness and sea ice coverage of the Arctic Ocean[16].

Despite being sparse in space and time, the available observations of Arctic Ocean eddies do indicate that eddies play a crucial role in Arctic halocline properties and marine ecosystems, specifically by transporting water masses with varying properties between Arctic continental shelves and the deep basin[17–19]. Eddy fluxes may also be one of the main factors influencing freshwater storage and circulation strength in the Beaufort Gyre[20,21], the largest freshwater reservoir in the Arctic, which is relevant to climate[22–25]. Sea ice, a unique feature in high latitudes, contributes to the dissipation of near-surface eddies and prevents their growth[26]. Sea ice decline may thus lead to an increase in Arctic eddy activity[26–29]. It has been argued that eddy activity in the western Arctic strengthened in response to increases in freshwater content over the past two decades on the basis of estimates of ocean energy budget[28]. At the same time, it was suggested that the increase of baroclinic instability and eddy activity in the Beaufort Gyre is relatively small due to the spatial expansion of the gyre during its spin-up[30]. There is therefore still a lack of consensus about current changes in eddy activity in the western Arctic. Long-term changes in eddy activity in other Arctic regions are even less well understood.

Over the past few decades, the lower atmosphere in the Arctic has been warming at an alarming rate[31,32]. At the same time, Arctic sea ice has undergone a notable decline[33,34]. Warming signals are also evident in various regions and depth ranges of the Arctic Ocean[35–39]. These marked changes in the atmosphere, sea ice and ocean in the Arctic are interrelated[40]. As the Arctic physical environment continues to change, there is reason to expect that the eddy activity in the Arctic will change

[1]Alfred Wegener Institute Helmholtz Center for Polar and Marine Research, Bremerhaven, Germany. [2]Constructor University, Bremen, Germany. [3]Department of Physics and Electrical Engineering, University of Bremen, Bremen, Germany. ✉e-mail: Qiang.Wang@awi.de
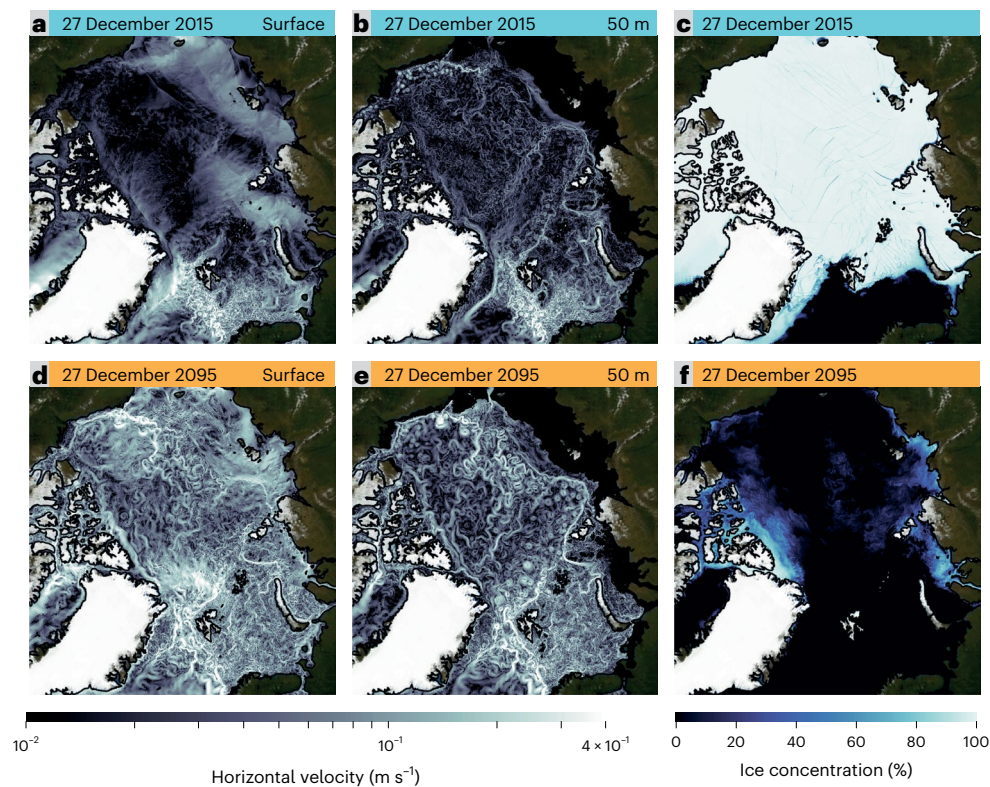
**Fig. 1 | Intensification of Arctic Ocean currents and eddy activity in a warming climate. a–f**, Snapshots of ocean currents and eddy activity at the surface (**a**,**d**) and at 50 m deep (**b**,**e**) from a global sea ice–ocean simulation with a resolution of 1 km in the Arctic. The right column shows the corresponding Arctic sea ice concentration (**c**,**f**). The upper row is for 27 December 2015 (present-day), and the bottom row is for 27 December 2095 (approximately +4 K warmer world). This figure is intended only for illustrative purposes; refer to other figures for quantitative representations of the changes in the ocean. Credit: background image, NASA Earth Observatory.

in concert. The level of understanding that the scientific community has about the evolution of Arctic Ocean eddy activity is not commensurate with the importance of Arctic climate change.

This study aims to help close the gap in the understanding of how and why Arctic Ocean eddy activity will change in a warming world. To achieve this, we used a global multi-resolution sea ice–ocean model (FESOM2)[41] to conduct simulations at two different resolutions in the Arctic Ocean: eddy-present (4.5 km) and eddy-rich (1 km). We quantified changes in Arctic eddy activity from the present to the end of the twenty-first century in a four-degree-warmer world and found that eddy activity in the upper Arctic Ocean will markedly intensify in the future—even more so than in eddy-rich regions of other parts of the world ocean.

## Long-term evolution of Arctic Ocean eddy activity

A strikingly clear picture of how Arctic Ocean eddy activity will change in a warming world can be obtained by examining randomly chosen daily snapshots of modelled ocean currents for the years 2015 and 2095. On 27 December 2015, for example, the Arctic basin is entirely covered by sea ice, whereas on 27 December 2095, there are only very small areas of sea ice remaining in the Arctic (Fig. 1c,f). In the presence of compact sea ice in 2015, eddy activity at the ocean surface is very low (Fig. 1a). This is because sea ice friction spins down existing surface eddies and prevents the growth of new ones[42]. At 50 m deep, coherent eddies are abundant along the Eurasian continental slope, in the Beaufort Sea, and in some areas of the deep basin in the present-day climate (Fig. 1b). This contrast in eddy activity between the surface and subsurface is typical for present-day conditions and, as we will see below, will change fundamentally in a +4 K warmer world. The velocity field on 27 December

2095 shows that small-scale motions are dramatically enhanced at the ocean surface, with velocity magnitudes similar to those at 50 m deep. Not only is the eddy velocity considerably intensified at the surface; it is also notably higher at a depth of 50 m than in 2015 (Fig. 1d,e). In the absence of sea ice cover, surface eddies are somehow smeared by winds, especially in the eastern Eurasian Basin and Canada Basin on the considered day (Fig. 1d).

In the eddy-present simulation, Arctic EKE in the upper 200 m experiences a striking, continuous increase throughout the twenty-first century (Fig. 2a) along with the well-known sea ice decline (Fig. 2d). EKE is projected to increase in both the Eurasian and Canada basins. By better resolving mesoscale eddies in the Arctic basin, the eddy-rich simulations show an even more pronounced increase in Arctic EKE. The mean EKE in the upper 200 m of the Arctic Ocean shows a significant trend of $(1.39 \pm 0.07) \times 10^{-4} \, \text{m}^2 \, \text{s}^{-2}$ per decade ($P < 0.01$) in the eddy-rich simulations over the three time slices (2012–2015, 2052–2055 and 2092–2095), while the trend in the eddy-present simulation calculated for the same periods is only about half, with a value of $(0.70 \pm 0.03) \times 10^{-4} \, \text{m}^2 \, \text{s}^{-2}$ per decade ($P < 0.01$). According to the eddy-rich simulations, the EKE in the upper 200 m for 2092–2095 is approximately three times higher than that for 2012–2015 in the Arctic Ocean and the Canada Basin, and about four times higher in the Eurasian Basin.

We observed a future increase in EKE in both the 0–100 m and 100–200 m depth layers, with the increase more pronounced in the upper layer (Extended Data Fig. 1a). Similarly, the mean EKE both in the surface mixed layer and above the halocline base depth exhibits an upward trend in a warming climate (Extended Data Fig. 1b). The increase in mean EKE is larger in the surface mixed layer, consistently showing that EKE increases more noticeably closer to the ocean surface. At the end of the twenty-first century, the Arctic surface EKE is expected to increase by approximately
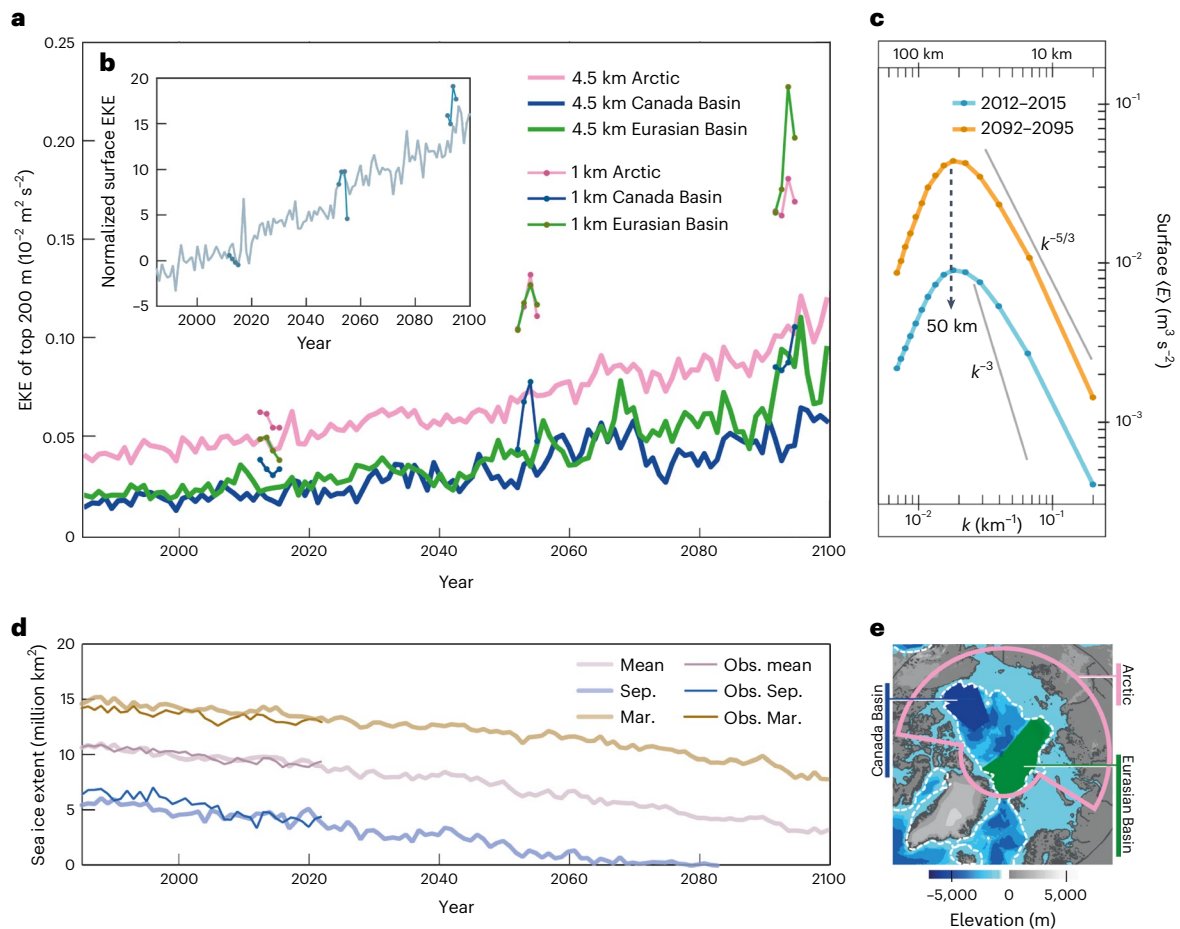
**Fig. 2 | Long-term changes in EKE, energy spectrum and sea ice extent. a**, Time series of mean EKE over the upper 200 m of the Arctic Ocean (pink), the Canada Basin (blue) and the Eurasian Basin (green) in the eddy-present simulation (solid lines) and in the three time-slice simulations with eddy-rich resolution (solid lines with circles; 2012–2015, 2052–2055 and 2092–2095). **b**, Change of surface EKE relative to the mean over 1985–2015 and normalized by the standard deviation of EKE in 1985–2015 from the eddy-present simulation (solid line) and eddy-rich simulations (solid lines with circles). **c**, Energy spectrum $<E>$ of Arctic Ocean surface currents as a function of filtering wavenumber $k$ in two periods of the eddy-rich simulations: 2012–2015 (cyan) and 2092–2095 (orange). **d**, Time series of annual mean, September and March sea ice extent in the Arctic Ocean in the eddy-present simulation (thick lines) and in observations (obs.) (thin lines, from the National Snow and Ice Data Center). The standard errors estimated for the observed annual, September and March sea ice extent are 0.012, 0.017 and 0.010 million km², respectively. **e**, Indication of analysed regions with bathymetry as the background: Arctic Ocean (pink), Canada Basin (blue) and Eurasian Basin (green). The white dashed line indicates the 500-metre isobath, which sets the southern boundary of the two deep basins.

15 times the standard deviation ($\sigma$) of the historical surface EKE in both the eddy-present and eddy-rich simulations (Fig. 2b).

## Eddy generation

In the present-day climate, EKE in the upper 200 m is higher in the Fram Strait, in the vicinity of the Eurasian continental slope, along the Lomonosov Ridge and in the southern Beaufort Sea and Barents Sea than in other Arctic regions (Fig. 3a). These well-known eddying regions are characterized by topographically steered currents of Atlantic and Pacific waters[30,43], where high conversion rates from eddy available potential energy to EKE ($T_{BC}$) are found (Fig. 3b). Our projections indicate that the regions with relatively high EKE in the current climate will experience the most pronounced increases in EKE (Fig. 3a,c). Consistent with the increases in EKE, $T_{BC}$ will increase most strongly in these regions (Fig. 3b,d and Extended Data Fig. 2a,b). In regions with relatively low eddy activity in the current climate, such as the Lincoln Sea, EKE and $T_{BC}$ are not projected to strongly increase.

$T_{BC}$ is projected to increase the most noticeably in the upper ocean (Extended Data Fig. 3). In a warmer world, the isopycnal slope in the upper 50 m of the northern Eurasian Basin will steepen due to the upper Arctic Ocean freshening in a warming climate (Extended Data Fig. 4a–g), which

can be partly attributed to sea ice meltwater and increased precipitation and river runoff[44–46]. In the latitude band of the Atlantic Water boundary current, where the increases in $T_{BC}$ and EKE are more pronounced, the isopycnal slope in the upper ocean is flatter during 2092–2095 (Extended Data Fig. 4a–g). This suggests that a future decrease in sea ice friction at the ocean surface can enhance eddy growth and the conversion of potential energy to EKE. This effect of sea ice decline has been previously demonstrated through linear instability analysis under varying ocean surface friction conditions[26]. Similar impacts of sea ice decline on eddy growth are also expected for the western Arctic.

The simulated increase in $T_{BC}$ in the Canada Basin is consistent with the increase in available potential energy due to the inflation of the Beaufort Gyre with low-salinity water (Extended Data Fig. 4h–n). The increase in freshwater storage in the Beaufort Gyre in a warming climate can be attributed to both the strengthening of the hydrological cycle and the modulation of surface ocean circulation by sea ice decline[47].

## Eddy killing

Ocean surface friction due to winds and sea ice can considerably dampen eddies and remove energy from the ocean on spatial scales where eddies are found—a phenomenon called eddy killing[26,48–50]. This raises the
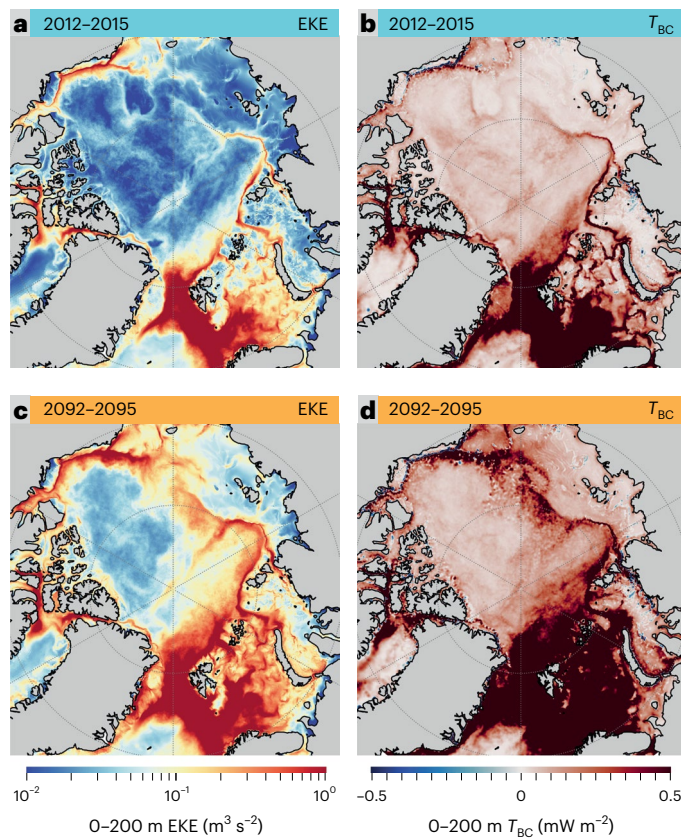
**Fig. 3 | Increase in EKE and baroclinicity in a warming world in eddy-rich simulations. a–d**, EKE (left) and $T_{BC}$ (right) integrated over the upper 200 m. The values for 2012–2015 are shown in **a**,**b**; those for 2092–2095 are shown in **c**,**d**.

question how the decline of Arctic sea ice will contribute to changes in EKE. To address this question, we evaluated the power input $EP_\ell^{Cg}$ (defined in equation (4) in Methods) that is associated with ocean surface stress induced by wind and sea ice. The kinetic energy spectrum for the surface ocean shows a peak at about 50 km for both the 2012–2015 and 2092–2095 periods (Fig. 2c). Also considering that Arctic surface eddies have a mean diameter of about 10 km (ref. 51), we take 50 km to approximate the upper bound of eddy scales. The $EP_\ell^{Cg}$ values at $\ell = 50$ km therefore represent eddy power induced by ocean surface stress.

During the months of February to May, most of the Arctic area is covered by compact sea ice with a concentration of over 90% in both the 2012–2015 and 2092–2095 periods, while the Arctic Ocean is projected to be nearly ice-free from August to November in 2092–2095 (Extended Data Fig. 5). Despite the lower sea ice concentration during February to May in 2092–2095 than in 2012–2015, perhaps somewhat counterintuitively, eddy killing becomes stronger (Fig. 4a). In fact, during this part of the year, EKE is removed at a rate of 0.17 mW m$^{-2}$ over the Arctic Ocean averaged in 2092–2095, which is about 40% higher than what is found for 2012–2015. The enhanced eddy killing can be explained by intensified eddy activity associated with a higher eddy generation rate. In other words, as long as sea ice is present that is still sufficiently compact to dissipate eddies, an increase in eddy generation will be accompanied by an increase in eddy killing. During August to November, eddy killing becomes weaker by 27% in 2092–2095 than in 2012–2015. This is because almost no sea ice is left during that part of the year in 2092–2095 (Extended Data Fig. 5). With sea ice absent, EKE is removed by winds, a process that has been found to be very important for the ocean energy budget along major currents of the world ocean[50].

The spatial patterns of $EP_\ell^{Cg}$ at the scale of 50 km demonstrate that eddy killing is strongest where the eddy generation rate and EKE

are high (Figs. 3 and 4b–e). The seasonal cycle in eddy killing is clearly enhanced in a warming climate, with strengthening in eddy killing during the ice-covered part of the year (Fig. 4b,d) and weakening from August to November (Fig. 4c,e). Although the surface power on scales smaller than 50 km is negative when averaged over the Arctic (Fig. 4a), it is positive in some shallow shelf seas when sea ice is absent (Fig. 4c,e). Note, in this context, that the baroclinic Rossby radius in the shelf seas is even smaller than in the Arctic deep basin[13]; therefore, in these areas, mesoscale eddies and thus the associated surface power are not properly resolved with 1 km resolution. Under climate warming, the annual average eddy killing in the Canada Basin and the eastern Eurasian Basin increases where the EKE becomes higher, and the increase does not show spatial correlation with changes in wind speeds (Extended Data Fig. 2). This indicates that the response of eddy killing to rising ocean eddy activity overshadows the impact of changes in wind speeds. Eddy killing weakens in certain regions with rising EKE, such as the western Eurasian Basin, because it also changes in response to sea ice decline.

## Eddy generation versus eddy killing

The difference in monthly $T_{BC}$ between 2012–2015 and 2092–2095 can explain the difference in the monthly EKE of the upper 200 m very well (Fig. 5a–f). Notably, the largest increase in the total EKE occurs in fall and winter, which corresponds to the largest rise in $T_{BC}$. The changes in eddy power ($EP_\ell^{Cg}$ at $\ell = 50$ km), which show increased eddy killing in winter and decreased eddy killing in fall, act to modulate the magnitude of the seasonal variability in the total EKE of the upper 200 m. The future increase in eddy power loss inside the Canada Basin is larger than that in $T_{BC}$ in winter, while the winter EKE is still projected to increase (Fig. 5c,f). This can be explained by strongly enhanced eddy generation near the shelf break in the western Arctic (Fig. 3). These shelf-break eddies shed into the Canada Basin, leading to an increase in eddy activity in the region[18].

By comparing the magnitudes of eddy power and EKE sources, it becomes evident that the Arctic Ocean eddies will undergo a regime shift in a warming world. In 2012–2015, $T_{BC}$ in the upper 200 m of the Arctic Ocean amounted to 0.10 mW m$^{-2}$, while the surface eddy power was about −0.09 mW m$^{-2}$. The similarity in their magnitudes reflects a regime of eddy activity predominantly controlled by sea ice. However, in 2092–2095, $T_{BC}$ is expected to increase to 0.26 mW m$^{-2}$, while the surface eddy power will amount to about −0.11 mW m$^{-2}$. The reduced ratio of surface eddy power to $T_{BC}$ indicates a regime reminiscent of what is currently found in the midlatitudes, where eddy killing is due to winds (not sea ice)[50]. The notable increase in the average $T_{BC}$ by a factor of 2.6, alongside an enhancement in the average eddy killing by approximately 20%, suggests that the main factor driving the future increase in Arctic Ocean eddy activity is the enhanced eddy generation rather than changes in eddy killing.

However, eddy killing by sea ice does dramatically influence eddy activity at the ocean surface. In both periods, the seasonal cycle of the surface EKE is highly correlated with sea ice area, but not with $T_{BC}$ (Extended Data Fig. 6), which demonstrates the direct impacts of sea ice friction on surface eddy activity. Therefore, while the future evolution of the mean EKE in the upper 200 m is to a larger extent determined by future increases in energy sources, the surface eddy activity will still be constrained by seasonal sea ice coverage. As a direct illustration, snapshots of ocean currents on 13 April in 2015 and 2095 indicate that surface eddy activity on both days is heavily suppressed by sea ice friction, even though eddy activity at 50 m deep is considerably higher in 2095 than in 2015 (Extended Data Fig. 7).

## Discussion

On the basis of new simulations with a kilometre-scale sea ice–ocean model, we show that Arctic EKE in the upper 200 m is projected to triple in a +4 K warmer world relative to current conditions. Long-term
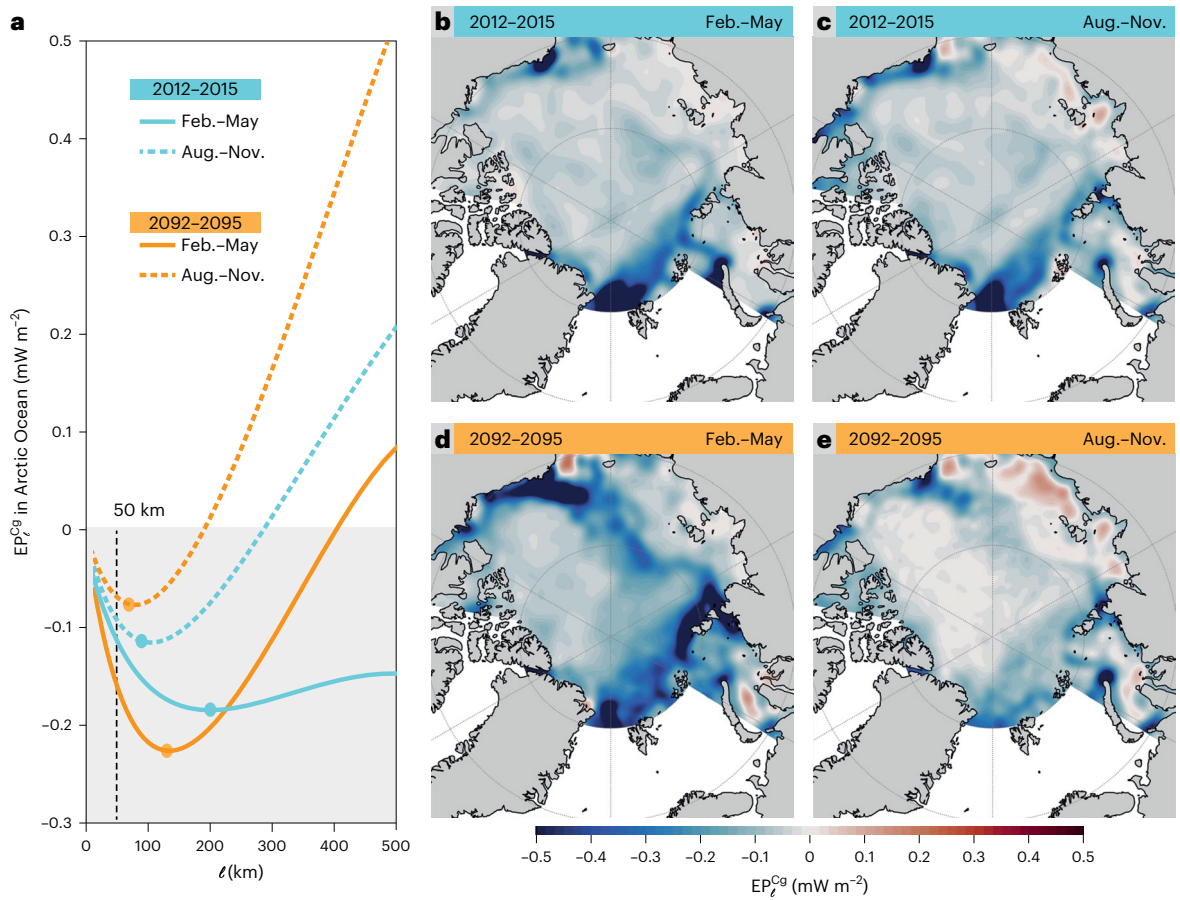
**Fig. 4 | Surface power input associated with ocean surface stress ($\mathrm{EP}_\ell^{\mathrm{Cg}}$) in eddy-rich simulations. a,** Arctic mean $\mathrm{EP}_\ell^{\mathrm{Cg}}$ as a function of spatial scales $\ell$ for 2012–2015 (cyan) and 2092–2095 (orange). Its value at the scale $\ell$ indicates the surface kinetic energy input on all scales smaller than $\ell$. The solid lines and the dashed lines represent the results for February to May and for August to November, respectively. The dots show the positions of minimum $\mathrm{EP}_\ell^{\mathrm{Cg}}$.

**b–e,** The spatial patterns of $\mathrm{EP}_\ell^{\mathrm{Cg}}$ at $\ell = 50$ km in February–May in 2012–2015 (**b**), August–November in 2012–2015 (**c**), February–May in 2092–2095 (**d**) and August–November in 2092–2095 (**e**). On the basis of the energy spectrum (Fig. 2c) and observed eddy size, we take $\ell = 50$ km as the upper bound of eddy scales, so **b–e** depict EKE loss (negative) due to surface stress in the deep basin area where mesoscale eddies are resolved with 1 km resolution.
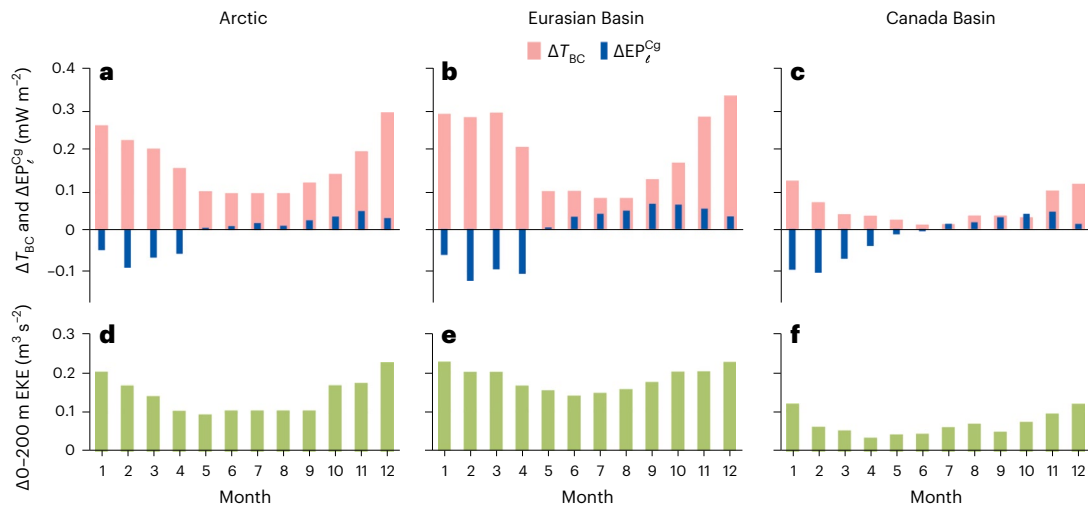


**Fig. 5 | Seasonal cycles of $T_{\mathrm{BC}}$, $\mathrm{EP}_\ell^{\mathrm{Cg}}$ and EKE in the upper 200 m in eddy-rich simulations. a–c,** The difference of $T_{\mathrm{BC}}$ integrated over upper 200 m (pink) and the surface power $\mathrm{EP}_\ell^{\mathrm{Cg}}$ at $\ell = 50$ km (blue) between the period 2092–2095 and the period 2012–2015 for the Arctic Ocean (**a**), the Eurasian Basin (**b**) and the Canada Basin (**c**). **d–f,** The difference of EKE over upper 200 m between the two periods for the Arctic Ocean (**d**), the Eurasian Basin (**e**) and the Canada Basin (**f**).

changes in EKE outside the Arctic Ocean are most pronounced in eddy-rich regions, such as the Antarctic Circumpolar Current, the Kuroshio Current and the Brazil and Malvinas currents[10]. The surface EKE in these regions was projected to increase by 3–6 times the standard deviation of the historical surface EKE ($\sigma$) in a +4 K warmer world[10]. We found that the surge in Arctic surface EKE amounts to approximately 15 times $\sigma$. This dramatic increase in the normalized surface EKE can be attributed to both the strong increase in surface EKE in the future and weak eddy activity and variability in the current climate. This suggests that a truly transformative increase in surface eddy activity will occur in the Arctic.

The driving mechanism behind the future increase in Arctic Ocean eddy activity is an increase in eddy generation rather than a decrease in eddy killing. The increase in eddy generation can be attributed to both the rise in available potential energy associated with the accumulation of freshwater and the reduction in sea ice cover, which facilitates eddy growth. Eddy killing, in contrast, exhibits differing behaviour across different seasons. In a warming climate, eddy killing tends to strengthen during the ice-covered part of the year and weaken in summer and fall. As a result, the annual mean eddy killing does not change much in the future. On the seasonal timescale, the seasonal cycle of sea ice cover remains the dominant factor influencing the seasonal variability of eddy activity at the ocean surface.

In the past, the Arctic Ocean was considered to be relatively 'quiescent' due to low variability associated with mesoscale eddies in the interior of the basin[16]. However, our results suggest that this region will experience much more energetic mesoscale variability and mean flows due to climate change. Considering the known impacts of Arctic eddies[18,19,28,29], the energized Arctic Ocean—which will come with intensified eddy transports of heat, carbon, oxygen and nutrients, and stronger modulation of heat and gas exchange between the ocean and atmosphere—could reshape the role of this region in climate and marine ecosystems. A better understanding of these changing processes is needed in future studies.

The quantitative results derived from our simulations have uncertainties due to, for example, the absence of atmosphere–ocean dynamic coupling, the use of constant ocean–ice drag coefficients and the relatively short length of the eddy-rich simulations. As a result, the future increase in Arctic Ocean eddy activity is probably underestimated in our simulations (see the discussions in Methods). To provide more accurate predictions regarding future changes in Arctic Ocean circulations on different spatial scales, dedicated efforts are required to reduce model uncertainties.

## Online content

Any methods, additional references, Nature Portfolio reporting summaries, source data, extended data, supplementary information, acknowledgements, peer review information; details of author contributions and competing interests; and statements of data and code availability are available at https://doi.org/10.1038/s41558-023-01908-w.

## References

1. Chelton, D. B., Schlax, M. G. & Samelson, R. M. Global observations of nonlinear mesoscale eddies. *Prog. Oceanogr.* **91**, 167–216 (2011).
2. Zhang, Z., Wang, W. & Qiu, B. Oceanic mass transport by mesoscale eddies. *Science* **345**, 322–324 (2014).
3. Dong, C., McWilliams, J. C., Liu, Y. & Chen, D. Global heat and salt transports by eddy movement. *Nat. Commun.* **5**, 3294 (2014).
4. Omand, M. M. et al. Eddy-driven subduction exports particulate organic carbon from the spring bloom. *Science* **348**, 222–225 (2015).
5. Conway, T. M., Palter, J. B. & de Souza, G. F. Gulf Stream rings as a source of iron to the North Atlantic subtropical gyre. *Nat. Geosci.* **11**, 594–598 (2018).
6. Zhai, X., Johnson, H. L. & Marshall, D. P. Significant sink of ocean-eddy energy near western boundaries. *Nat. Geosci.* **3**, 608–612 (2010).
7. Hewitt, H., Fox-Kemper, B., Pearson, B., Roberts, M. & Klocke, D. The small scales of the ocean may hold the key to surprises. *Nat. Clim. Change* **12**, 496–499 (2022).
8. Wang, H., Qiu, B., Liu, H. & Zhang, Z. Doubling of surface oceanic meridional heat transport by non-symmetry of mesoscale eddies. *Nat. Commun.* **14**, 5460 (2023).
9. Martínez-Moreno, J. et al. Global changes in oceanic mesoscale currents over the satellite altimetry record. *Nat. Clim. Change* **11**, 397–403 (2021).
10. Beech, N. et al. Long-term evolution of ocean eddy activity in a warming world. *Nat. Clim. Change* **12**, 910–917 (2022).
11. Newton, J., Aagaard, K. & Coachman, L. Baroclinic eddies in the Arctic Ocean. *Deep Sea Res. Oceanogr. Abstr.* **21**, 707–719 (1974).
12. Hunkins, K. L. Subsurface eddies in the Arctic Ocean. *Deep Sea Res. Oceanogr. Abstr.* **21**, 1017–1033 (1974).
13. Nurser, A. J. G. & Bacon, S. The Rossby radius in the Arctic Ocean. *Ocean Sci.* **10**, 967–975 (2014).
14. Zhao, M. et al. Characterizing the eddy field in the Arctic Ocean halocline. *J. Geophys. Res. Oceans* **119**, 8800–8817 (2014).
15. Zhao, M. & Timmermans, M.-L. Vertical scales and dynamics of eddies in the Arctic Ocean's Canada Basin. *J. Geophys. Res. Oceans* **120**, 8195–8209 (2015).
16. von Appen, W.-J. et al. Eddies and the distribution of eddy kinetic energy in the Arctic Ocean. *Oceanography* **35**, 42–51 (2022).
17. Pickart, R. S., Weingartner, T. J., Pratt, L. J., Zimmermann, S. & Torres, D. J. Flow of winter-transformed Pacific water into the Western Arctic. *Deep Sea Res. Part II Top. Stud. Oceanogr.* **52**, 3175–3198 (2005).
18. Spall, M. A., Pickart, R. S., Fratantoni, P. S. & Plueddemann, A. J. Western Arctic shelfbreak eddies: formation and transport. *J. Phys. Oceanogr.* **38**, 1644–1668 (2008).
19. Watanabe, E. et al. Enhanced role of eddies in the Arctic marine biological pump. *Nat. Commun.* **5**, 3950 (2014).
20. Manucharyan, G. E. & Spall, M. A. Wind-driven freshwater buildup and release in the Beaufort Gyre constrained by mesoscale eddies. *Geophys. Res. Lett.* **43**, 273–282 (2016).
21. Meneghello, G., Marshall, J., Campin, J.-M., Doddridge, E. & Timmermans, M.-L. The ice-ocean governor: ice-ocean stress feedback limits Beaufort Gyre spin-up. *Geophys. Res. Lett.* **45**, 11293–11299 (2018).
22. Morison, J. et al. Changing Arctic Ocean freshwater pathways. *Nature* **481**, 66–70 (2012).
23. Giles, K. A., Laxon, S. W., Ridout, A. L., Wingham, D. J. & Bacon, S. Western Arctic Ocean freshwater storage increased by wind-driven spin-up of the Beaufort Gyre. *Nat. Geosci.* **5**, 194–197 (2012).
24. Proshutinsky, A. et al. Analysis of the Beaufort Gyre freshwater content in 2003–2018. *J. Geophys. Res. Oceans* **124**, 9658–9689 (2019).
25. Zhang, J. et al. Labrador Sea freshening linked to Beaufort Gyre freshwater release. *Nat. Commun.* **12**, 1229 (2021).
26. Meneghello, G. et al. Genesis and decay of mesoscale baroclinic eddies in the seasonally ice-covered interior Arctic Ocean. *J. Phys. Oceanogr.* **51**, 115–129 (2021).
27. Zhao, M., Timmermans, M.-L., Cole, S., Krishfield, R. & Toole, J. Evolution of the eddy field in the Arctic Ocean's Canada Basin, 2005–2015. *Geophys. Res. Lett.* **43**, 8106–8114 (2016).
28. Armitage, T. W. K., Manucharyan, G. E., Petty, A. A., Kwok, R. & Thompson, A. F. Enhanced eddy activity in the Beaufort Gyre in response to sea ice loss. *Nat. Commun.* **11**, 761 (2020).
29. Manucharyan, G. E. & Thompson, A. F. Heavy footprints of upper-ocean eddies on weakened Arctic sea ice in marginal ice zones. *Nat. Commun.* **13**, 2147 (2022).

30. Regan, H., Lique, C., Talandier, C. & Meneghello, G. Response of total and eddy kinetic energy to the recent spinup of the Beaufort Gyre. *J. Phys. Oceanogr.* **50**, 575–594 (2020).

31. Screen, J. A. & Simmonds, I. The central role of diminishing sea ice in recent Arctic temperature amplification. *Nature* **464**, 1334–1337 (2010).

32. Rantanen, M. et al. The Arctic has warmed nearly four times faster than the globe since 1979. *Commun. Earth Environ.* **3**, 168 (2022).

33. Comiso, J. C., Meier, W. N. & Gersten, R. Variability and trends in the Arctic sea ice cover: results from different techniques. *J. Geophys. Res. Oceans* **122**, 6883–6900 (2017).

34. Kwok, R. Arctic sea ice thickness, volume, and multiyear ice coverage: losses and coupled variability (1958–2018). *Environ. Res. Lett.* **13**, 105005 (2018).

35. Li, Z., Ding, Q., Steele, M. & Schweiger, A. Recent upper Arctic Ocean warming expedited by summertime atmospheric processes. *Nat. Commun.* **13**, 362 (2022).

36. Lind, S., Ingvaldsen, R. B. & Furevik, T. Arctic warming hotspot in the northern Barents Sea linked to declining sea-ice import. *Nat. Clim. Change* **8**, 634–639 (2018).

37. Polyakov, I. V. et al. Greater role for Atlantic inflows on sea-ice loss in the Eurasian Basin of the Arctic Ocean. *Science* **356**, 285–291 (2017).

38. Shu, Q. et al. Arctic Ocean amplification in a warming climate in CMIP6 models. *Sci. Adv.* **8**, eabn9755 (2022).

39. Timmermans, M.-L., Toole, J. & Krishfield, R. Warming of the interior Arctic Ocean linked to sea ice losses at the basin margins. *Sci. Adv.* **4**, eaat6773 (2018).

40. Shu, Q., Wang, Q., Song, Z. & Qiao, F. The poleward enhanced Arctic Ocean cooling machine in a warming climate. *Nat. Commun.* **12**, 2966 (2021).

41. Danilov, S., Sidorenko, D., Wang, Q. & Jung, T. The Finite-volumE Sea ice–Ocean Model (FESOM2). *Geosci. Model Dev.* **10**, 765–789 (2017).

42. Ou, H. W. & Gordon, A. L. Spin-down of baroclinic eddies under sea ice. *J. Geophys. Res. Oceans* **91**, 7623–7630 (1986).

43. Wang, Q. et al. Eddy kinetic energy in the Arctic Ocean from a global simulation with a 1-km Arctic. *Geophys. Res. Lett.* **47**, e2020GL088550 (2020).

44. Carmack, E. C. et al. Freshwater and its role in the Arctic Marine System: sources, disposition, storage, export, and physical and biogeochemical consequences in the Arctic and global oceans. *J. Geophys. Res. Biogeosci.* **121**, 675–717 (2016).

45. Zanowski, H., Jahn, A. & Holland, M. M. Arctic Ocean freshwater in CMIP6 ensembles: declining sea ice, increasing ocean storage and export. *J. Geophys. Res. Oceans* **126**, e2020JC016930 (2021).

46. Wang, S., Wang, Q., Wang, M., Lohmann, G. & Qiao, F. Arctic Ocean freshwater in CMIP6 coupled models. *Earths Future* **10**, e2022EF002878 (2022).

47. Wang, Q. & Danilov, S. A. Synthesis of the upper Arctic Ocean circulation during 2000–2019: understanding the roles of wind forcing and sea ice decline. *Front. Mar. Sci.* **9**, 863204 (2022).

48. Renault, L., Molemaker, M. J., Gula, J., Masson, S. & McWilliams, J. C. Control and stabilization of the Gulf Stream by oceanic current interaction with the atmosphere. *J. Phys. Oceanogr.* **46**, 3439–3453 (2016).

49. Gupta, M., Marshall, J., Song, H., Campin, J.-M. & Meneghello, G. Sea-ice melt driven by ice-ocean stresses on the mesoscale. *J. Geophys. Res. Oceans* **125**, e2020JC016404 (2020).

50. Rai, S., Hecht, M., Maltrud, M. & Aluie, H. Scale of oceanic eddy killing by wind from global satellite observations. *Sci. Adv.* **7**, eabf4920 (2021).

51. Kozlov, I. E., Artamonova, A. V., Manucharyan, G. E. & Kubryakov, A. A. Eddies in the western Arctic Ocean from spaceborne SAR observations over open ocean and marginal ice zones. *J. Geophys. Res. Oceans* **124**, 6601–6616 (2019).

## Methods

### Description of model simulations

We employed the Finite-Volume Sea Ice–Ocean Model version 2 (FESOM2), which is a global ocean general circulation model formulated on unstructured triangular grids[41]. It performs similarly to its predecessor version in simulating the global ocean and sea ice but has a much higher computational efficiency[52–54]. Past studies have successfully utilized FESOM2 to study mesoscale eddy activity in the Arctic Ocean[16,43]. Its unstructured grids allow one to use variable resolution and concentrate computational resources in chosen regions, thus reducing the overall computational cost.

Two model configurations were used in this study. The first one resolves mesoscale eddies in the deep basin area of the Arctic Ocean. It has a horizontal resolution of 1 km in the Arctic Ocean and 30 km elsewhere, and 70 unevenly spaced vertical layers with 5 m resolution in the upper 100 m. The second one is marginally eddy permitting in the Arctic Ocean. It has a horizontal resolution of 4.5 km in the Arctic Ocean and 48 vertical layers. The second configuration, although relatively coarse, is much finer than state-of-the-art CMIP6 models, which have a typical ocean resolution of about 30 to 50 km in the Arctic. We call the simulation using 1 km resolution the 'eddy-rich simulation' and the one using 4.5 km resolution the 'eddy-present simulation'.

We first performed the eddy-present simulation from 1958 to 2100 starting from the Polar Science Center Hydrographic Climatology dataset (PHC3.0)[55]. We then interpolated the ocean and sea ice model results at the end of 2009, 2049 and 2089 obtained from the eddy-present simulation onto the 1-km-resolution model grid. Three time slices of the eddy-rich simulation were performed starting from these initial conditions separately for six model years each—that is, 2010 to 2015, 2050 to 2055 and 2090 to 2095. The first two years of each time slice were considered a re-spin-up, and the last four years were used in our analysis.

The atmospheric forcing and river runoff used to drive the simulations were derived from the CMIP6 simulation result of the coupled climate model AWI-CM[56], comprising the historical period (1958–2014) and the SSP585 future scenario (2015–2100)[57]. This CMIP6 simulation reasonably reproduced the past climate in its historical period[58], including air temperature in the Arctic region[59]. In the SSP585 scenario, this CMIP6 simulation projects that the global mean surface air temperature will increase by around 4 K in the 2090s above the 2000–2015 level[58], very similar to the multi-model-mean result of CMIP6 models[60]. With this forcing, our FESOM2 simulation can well reproduce the satellite-observed decline in Arctic sea ice extent (Fig. 2d). The Arctic Ocean will become ice-free (having less than one million square kilometres of sea ice) in September in the 2050s in our simulation, consistent with the CMIP6 multi-model-mean result[61]. The atmospheric forcing fields have a spatial resolution of T127 (about 100 km in the meridional direction; about 100 km at the Equator and 27 km at 75° N in the zonal direction) and a temporal resolution of three hours.

In our simulations, the calculation of wind stress incorporates the relative motion between wind and ocean surface speed. For consistency with the AWI-CM simulations, we used constant ice–ocean and ice–air drag coefficients. The implications of employing forced sea ice–ocean model simulations and constant sea ice drag coefficients for the representation of eddy activity are discussed below in the section on the uncertainty in model simulations.

### Calculation of EKE

The Reynolds averaging method can be used to split the total kinetic energy (TKE) of a fluid flow into its mean kinetic energy (MKE) and EKE components. The MKE represents the energy associated with the mean flow, while the EKE represents the energy associated with the turbulent or eddy fluctuations in the flow. Ocean velocity can be decomposed into a time mean (indicated by overbars) and an eddy part (indicated by primes), $\mathbf{u} = (u, v) = (\bar{u} + u', \bar{v} + v')$. EKE is then calculated as the following:

$$\text{EKE} = \text{TKE} - \text{MKE} = \frac{1}{2}(\overline{u^2} + \overline{v^2}) - \frac{1}{2}(\bar{u}^2 + \bar{v}^2) = \frac{1}{2}(\overline{u'^2} + \overline{v'^2}). \quad (1)$$

$\overline{u^2}$ and $\overline{v^2}$ are monthly means obtained directly from model output. $\bar{u}$ and $\bar{v}$ are seasonal three-month means. Using longer-period running means would add seasonal variability of kinetic energy to EKE.

Besides calculating mean EKE in fixed depth ranges, we also calculated mean EKE in the surface mixed layer and in the depth range above the halocline base depth (Extended Data Fig. 2). The calculation of mixed layer depth and halocline base depth follows previous studies[62,63] as explained in Extended Data Fig. 2.

Although Reynolds averaging is the most popularly used method to calculate EKE, it categorizes high-frequency variability of surface currents, induced directly by high-frequency wind variability, as eddy signals. To address this issue, we employed the coarse-graining method[64] to decompose kinetic energy into different spatial scales, considering only the kinetic energy on scales smaller than 50 km as EKE (see the details in the section on 'Energy spectrum' below). The coarse-graining method also has its limitations. It requires the selection of a spatial scale threshold to determine the EKE, and in our case, we chose the location of the maximum in the energy spectrum. While most of the observed Arctic Ocean eddies are smaller than 50 km, there are some that exceed this scale. If we were to use a larger threshold, a portion of the kinetic energy associated with mean currents would be included in the EKE calculation. Both methods therefore offer approximate estimations of EKE. Considering the nature of high-frequency wind variability and the potential for overestimation of ocean surface EKE using the Reynolds averaging method, the coarse-graining method provides a more accurate quantification of ocean surface EKE, given that the majority of Arctic eddies are smaller than 50 km.

We found that the magnitude of the seasonal variability of Arctic surface EKE is considerably overestimated with the Reynolds averaging method compared with the result obtained with the coarse-graining method (Extended Data Fig. 8a,b). We therefore show the seasonal ocean surface EKE calculated using the coarse-graining method in Extended Data Fig. 6a–c. We also found that with either calculation method, the long-term trend of EKE remains statistically significant and is not obscured by seasonal variability.

We also calculated normalized ocean surface EKE as done in the previous study on future EKE changes in lower latitudes[10]:

$$\text{EKE}_{\text{normalized}} = \frac{\text{EKE} - \overline{\text{EKE}_{\text{hist}}}}{\sigma}, \quad (2)$$

where $\overline{\text{EKE}_{\text{hist}}}$ represents the mean EKE in the historical period of 1985–2014 in the eddy-present simulation and the mean EKE in 2012–2015 in the eddy-rich simulation. $\sigma$ refers to the standard deviation of EKE in the historical period of 1985–2014 in the eddy-present simulation and the range (maximum minus minimum) of EKE in 2012–2015 in the eddy-rich simulation. The latter is taken as an approximation of EKE variability because the time-slice simulation is too short to be used to compute standard deviation. In the eddy-present simulation, the range of EKE in 2012–2015 is larger than the standard deviation in 1985–2014, so the normalized EKE in the eddy-rich simulation might be underestimated in our approximation. The normalized ocean surface EKE is about 15 by the end of the twenty-first century in both the eddy-present and eddy-rich simulations (Fig. 2b), indicating that the increase in surface EKE is at least 15 times the historical magnitude of EKE interannual variability.

### Eddy killing

To quantify the surface flux of kinetic energy associated with eddies and ocean surface stress (also called eddy power), one way is to use Reynolds averaging:

$$\text{EP}^{\text{Rey}} = \overline{\boldsymbol{\tau} \cdot \mathbf{u}} - \overline{\boldsymbol{\tau}} \cdot \overline{\mathbf{u}} = \overline{\boldsymbol{\tau}' \cdot \mathbf{u}'}, \qquad (3)$$

where $\boldsymbol{\tau}$ is ocean surface stress, $\mathbf{u}$ is ocean surface velocity, overbars indicate temporal means and primes indicate temporal fluctuations. As shown in Extended Data Fig. 8c,d, this traditional measure $\text{EP}^{\text{Rey}}$ is positive in many areas, even in the current climate conditions with year-round sea ice cover in the central Arctic, thus failing to capture eddy killing. It has been noticed that this measure also cannot capture eddy killing by winds in other parts of the world ocean[50].

We therefore used spatial averaging to diagnose eddy killing as suggested by ref. [50]:

$$\text{EP}^{\text{Cg}}_{\ell} = \langle \boldsymbol{\tau} \cdot \mathbf{u} \rangle_{\ell} - \langle \boldsymbol{\tau} \rangle_{\ell} \cdot \langle \mathbf{u} \rangle_{\ell}, \qquad (4)$$

where $\langle \ldots \rangle_{\ell}$ represents low-pass filtering in space, which is practically realized through applying coarse-graining with the filter scale $\ell$. $\text{EP}^{\text{Cg}}_{\ell}$ represents the surface kinetic energy flux on scales smaller than $\ell$. When $\ell$ is the spatial scale representing the upper bound of eddy size for most of the eddies, then the corresponding $\text{EP}^{\text{Cg}}_{\ell}$ can be considered eddy power input by surface stress. A negative value indicates that EKE is removed and eddies are killed. As shown in Fig. 4b–e, eddy power $\text{EP}^{\text{Cg}}_{\ell}$ is predominantly negative, successfully demonstrating eddy killing by ocean surface stress.

Averaging $\text{EP}^{\text{Cg}}_{\ell}$ over the Arctic Ocean for each filter scale $\ell$, we can get Arctic mean $\text{EP}^{\text{Cg}}_{\ell}$ as a function of the filter scale as shown in Fig. 4a. On average, on spatial scales smaller than the threshold scale corresponding to the minimum value of $\text{EP}^{\text{Cg}}_{\ell}$, kinetic energy is removed from the ocean. On scales larger than the threshold scale, the ocean gains kinetic energy from surface stress.

We calculated equation (4) using daily ocean surface stress and ocean surface velocity data from the model. We saved total ocean surface stress on each model grid cell but did not output its proportions under sea ice and in the open ocean on each model grid cell separately. Therefore, $\text{EP}^{\text{Cg}}_{\ell}$ is the ocean surface kinetic energy flux associated with the total surface stress. We note that the individual contributions from sea ice and open ocean (direct winds) on each model grid cell to $\text{EP}^{\text{Cg}}_{\ell}$ cannot be rationally separated even when we have surface stress proportions under sea ice and in the open ocean on each model grid cell separately, because the ocean surface velocity $\mathbf{u}$ on the model grid cell is influenced by the total ocean surface stress in the coupled sea ice–ocean system.

The above-mentioned technical issue does not prevent us from understanding changes in eddy killing associated with sea ice decline. We chose a season (February to May) when most of the Arctic Ocean area is covered by relatively compact (over 90% concentration) sea ice in both 2012–2015 and 2092–2095 (Extended Data Fig. 5). The eddy killing in this season can be considered to be mainly associated with sea ice cover. The other season chosen is from August to November, which features a sea ice concentration of about 80% on average in 2012–2015 and is ice-free in 2092–2095 (Extended Data Fig. 5). The difference in eddy killing in this season between the two climate scenarios can be considered a change from eddy killing dominated by sea ice to eddy killing just by winds. Sea ice concentration influences the surface kinetic energy flux not only through the relative contributions from sea ice and direct winds but also through the compactness and immobility of sea ice. Sea ice internal stress is an exponential function of sea ice concentration, which explains the very low, negative $\text{EP}^{\text{Cg}}_{\ell}$ values even on large spatial scales in February to May in 2012–2015 (Fig. 4a). The compact winter sea ice in these months blocks kinetic energy input to the ocean even on large spatial scales.

## Energy spectrum
To estimate the spatial scales of surface eddies, we calculated spectral energy density. The kinetic energy contained in spatial scales larger than $\ell$ is

$$\mathscr{E} = \frac{1}{2} |\langle \mathbf{u} \rangle_{\ell}|^2. \qquad (5)$$

By differentiating the coarse kinetic energy $\mathscr{E}$, we can get kinetic energy content at different scales—that is, the spectral energy density[65,66]

$$\langle E(k_{\ell}) \rangle = \frac{\mathrm{d}}{\mathrm{d}k_{\ell}} \{\mathscr{E}\} = -\ell^2 \frac{\mathrm{d}}{\mathrm{d}\ell} \{\mathscr{E}\}, \qquad (6)$$

where $k_{\ell} = 1/\ell$ is the filtering wavenumber and $\{\cdot\}$ represents spatial averaging. As shown in ref. [65], $\langle E(k_{\ell}) \rangle$ is equivalent to the traditional Fourier spectrum when applying Fourier analysis is possible. Daily velocity is used in the above analysis.

Extended Data Fig. 9 depicts the power spectral density for the Arctic surface kinetic energy for 2012–2015 (dashed blue line) and 2092–2095 (dashed red line). In both periods, the spectrum does not show a peak that allows us to identify the spatial scale of mesoscale eddies. The reason is that the width of the circumpolar boundary current has a scale with a lower bound close to 100 km, which masks the upper spatial scale of mesoscale eddies in the spectrum. When we remove the coarse energy on scales larger than 100 km before calculating the spectrum, the peaks emerge, located at about 50 km in both periods (Extended Data Fig. 9, solid lines; also in Fig. 2c). Reinforced by the fact that observed Arctic eddies have a typical size of about 10 km in diameter[51], we take 50 km as the eddy scale below which surface kinetic energy flux (that is, $\text{EP}^{\text{Cg}}_{\ell=50\text{km}}$) is considered to be associated with eddies.

As depicted in Fig. 4a, the threshold scales corresponding to the minimum $\text{EP}^{\text{Cg}}_{\ell}$ values are larger than 50 km. In ice-free months in 2092–2095, the threshold scale is 60 km and close to the eddy scale we estimated. This supports previous studies on eddy killing in lower latitudes that simply took the threshold value as the eddy scale[50]. In the seasons with sea ice cover in the Arctic Ocean, the threshold scale corresponding to the minimum $\text{EP}^{\text{Cg}}_{\ell}$ values is not a proper approximation for eddy scales.

## Coarse-graining method
In this study, we applied the coarse-graining method to compute $\text{EP}^{\text{Cg}}_{\ell}$ and energy spectrum as described above. For a field $\varphi(\mathbf{x})$, its coarse-grained field can be obtained via

$$\langle \varphi_{\ell}(\mathbf{x}) \rangle = G_{\ell} * \varphi(\mathbf{x}), \qquad (7)$$

which involves convolution ($*$) and a normalized filter kernel $G_{\ell}(\mathbf{r})$[64]. The above equation can be interpreted as a spatial average over an area of diameter $\ell$ centred at $\mathbf{x}$, so $\langle \varphi_{\ell}(\mathbf{x}) \rangle$ contains only length scales larger than $\ell$. The filter kernel is defined as

$$G_{\ell}(\mathbf{r}) = A \frac{1}{2} \left( 1 - \tan h \frac{|\mathbf{r}| - \frac{\ell}{2}}{L_0} \right), \qquad (8)$$

where $L_0$ is set to 2 km considering our horizontal resolution of 1 km. The normalization factor $A$ ensures $\sum G_{\ell}(\mathbf{r}) = 1$.

## Energy conversion rate
The conversion rate from eddy available potential energy to EKE is calculated using Reynolds averaging[67]:

$$T_{\text{BC}} = -g\overline{w'\rho'}, \qquad (9)$$

where $g$ is the acceleration of gravity, $w'$ is the temporal fluctuation from the mean vertical velocity and $\rho'$ is the temporal fluctuation from the mean density.

There is no well-established dynamic framework for diagnosing eddy conversion rates using spatial averaging, so we still use the

temporal averaging as in equation (9) in this study. A comparison between $T_{BC}$ based on temporal averaging and eddy killing $EP_{\ell}^{Cg}$ based on spatial averaging does not allow us to fully close the budget for EKE. However, as argued in ref. 50, comparing these two terms can still inform us on how important eddy killing is.

## Calculation of linear trend

The linear trend of the top 200 m mean EKE in the Arctic Ocean was determined by analysing the annual mean EKE in 12 years (2012 to 2015, 2052 to 2055 and 2092 to 2095) for both the eddy-rich and eddy-present simulations. By using the same years for estimating the linear trend in both simulations, we can make a direct and fair comparison between them. To evaluate the statistical significance of the linear trend, we calculated the $P$ value on the basis of the $t$ statistic for the two-sided hypothesis test.

## Changes and impacts of mean energy

Not only will the Arctic Ocean EKE increase in a warming climate, but its MKE will increase as well (Extended Data Fig. 10). Overall, this results in an increase in TKE. The increase in MKE can be attributed in part to enhanced surface kinetic energy input from the atmosphere to the Arctic Ocean. Figure 4a illustrates that the ocean gains kinetic energy starting from smaller spatial scales in 2092–2095 compared with 2012–2015, with the magnitude of surface kinetic energy input on large scales being larger in 2092–2095, especially in the ice-free season. In the CMIP6 atmospheric forcing used in our study, Arctic average wind speeds for 2092–2095 are about 12% larger than for 2012–2015, which can contribute to the enhanced surface kinetic energy input across the Arctic. However, the future kinetic energy input on large scales is estimated to be more than twice that in the current climate conditions (Fig. 4a). We therefore propose sea ice decline to be the primary reason for the future increase in surface kinetic energy input. Part of the MKE could convert to mean available potential energy, indirectly contributing to the increase in EKE[67].

We also found that the energy conversion rate from MKE to EKE averaged in the Arctic Ocean is negative, indicating energy transfer from mesoscales to mean flows. This transfer will become larger in 2092–2095 than in 2012–2015, but its difference between these two periods is approximately seven times smaller than the difference in $T_{BC}$.

## Uncertainty in model simulations

Sea ice and the ocean are dynamically coupled in the model, so eddy killing by sea ice is consistently simulated. However, the atmosphere is not dynamically coupled with the ocean, and the EKE lost to the atmosphere cannot be seen by the ocean again in our forced simulations. This could result in overestimation of eddy killing by winds[48]. Therefore, quantitatively, our simulated future increase in Arctic eddy activity represents the lower bound of possible future increases for the considered climate scenario. Considering that the simulated EKE can be underestimated by about 30% without the atmospheric feedback[68], and on average during half of the time eddy killing is dominated by direct wind stress in the Arctic in 2092–2095, we estimate that the EKE in the upper 200 m in 2092–2095 (15% higher than the simulated value) is about 3.5 times the EKE in 2012–2015, instead of 3 times as estimated in the main text. Despite this possible underestimation, our simulations provide a first-order estimate for future Arctic Ocean eddy activity changes under sea ice decline. Parameterizations for ocean current feedback in forced simulations have been suggested before[68], but the parameters are valid for non-polar seas. Parameterizations suitable for partially ice-covered model grid cells are warranted to help improve model representation of air–ocean coupling in forced simulations.

The eddy-rich simulations were initialized from the results of the eddy-present simulations, and only two years of eddy-rich simulations in each period were considered as a model re-spin-up. The relatively short re-spin-up period might cause some uncertainties in the analysed model results.

Observations indicate that there is a considerable level of uncertainty in the estimates of drag coefficients[69], and larger uncertainty is expected in the future changes in sea ice roughness and ice–ocean drag coefficients. Using constant sea ice drag coefficients is currently a common practice in climate simulations, but previous studies suggest that the reduction in sea ice roughness associated with thinner sea ice could lead to a decrease in ice–ocean stress and momentum transfer[70]. This reduction in ocean surface friction may weaken eddy killing and promote eddy growth. Therefore, because we used constant ice–ocean drag coefficients in our simulations, we may have underestimated future increases in eddy activity in the Arctic Ocean. However, the reduction in overall momentum transfer to the ocean associated with thinner sea ice could also indirectly affect eddy activity through its influence on ocean circulation and water mass distribution. It is necessary to improve ice–ocean drag coefficient and sea ice roughness parameterizations (particularly under low-ice-concentration conditions[69,71]) and apply them in model simulations, thus ultimately reducing uncertainties in the simulations.

## Data availability

The model data used to produce the paper figures are available at https://doi.org/10.5281/zenodo.10020010 (ref. 72).

## Code availability

The model code used for the simulations is available at https://doi.org/10.5281/zenodo.4742242 (ref. 73).

## References

52. Scholz, P. et al. Assessment of the Finite-volumE Sea ice–Ocean Model (FESOM2.0)—part 1: description of selected key model elements and comparison to its predecessor version. *Geosci. Model Dev.* **12**, 4875–4899 (2019).
53. Scholz, P. et al. Assessment of the Finite-VolumE Sea ice–Ocean Model (FESOM2.0)—part 2: partial bottom cells, embedded sea ice and vertical mixing library CVMix. *Geosci. Model Dev.* **15**, 335–363 (2022).
54. Koldunov, N. V. et al. Scalability and some optimization of the Finite-volumE Sea ice–Ocean Model, Version 2.0 (FESOM2). *Geosci. Model Dev.* **12**, 3991–4012 (2019).
55. Steele, M., Morley, R. & Ermold, W. PHC: a global ocean hydrography with a high-quality Arctic Ocean. *J. Clim.* **14**, 2079–2087 (2001).
56. Sidorenko, D. et al. Towards multi-resolution global climate modeling with ECHAM6–FESOM. Part I: model formulation and mean climate. *Clim. Dyn.* **44**, 757–780 (2015).
57. O'Neill, B. C. et al. The Scenario Model Intercomparison Project (ScenarioMIP) for CMIP6. *Geosci. Model Dev.* **9**, 3461–3482 (2016).
58. Semmler, T. et al. Simulations for CMIP6 with the AWI climate model AWI-CM-1-1. *J. Adv. Model. Earth Syst.* **12**, e2019MS002009 (2020).
59. Cai, Z. et al. Arctic warming revealed by multiple CMIP6 models: evaluation of historical simulations and quantification of future projection uncertainties. *J. Clim.* **34**, 4871–4892 (2021).
60. Brunner, L. et al. Reduced global warming from CMIP6 projections when weighting models by performance and independence. *Earth Syst. Dyn.* **11**, 995–1012 (2020).
61. Notz, D. & SIMIP Community. Arctic sea ice in CMIP6. *Geophys. Res. Lett.* **47**, e2019GL086749 (2020).
62. Peralta-Ferriz, C. & Woodgate, R. A. Seasonal and interannual variability of pan-Arctic surface mixed layer properties from 1979 to 2012 from hydrographic data, and the dominance of stratification for multiyear mixed layer depth shoaling. *Prog. Oceanogr.* **134**, 19–53 (2015).
63. Bourgain, P. & Gascard, J. The Arctic Ocean halocline and its interannual variability from 1997 to 2008. *Deep Sea Res. 1 Oceanogr. Res. Pap.* **58**, 745–756 (2011).

64. Aluie, H., Hecht, M. & Vallis, G. K. Mapping the energy cascade in the North Atlantic Ocean: the coarse-graining approach. *J. Phys. Oceanogr.* **48**, 225–244 (2018).

65. Storer, B. A., Buzzicotti, M., Khatri, H., Griffies, S. M. & Aluie, H. Global energy spectrum of the general oceanic circulation. *Nat. Commun.* **13**, 5314 (2022).

66. Sadek, M. & Aluie, H. Extracting the spectrum of a flow by spatial filtering. *Phys. Rev. Fluids* **3**, 124610 (2018).

67. von Storch, J.-S. et al. An estimate of the Lorenz energy cycle for the world ocean based on the STORM/NCEP simulation. *J. Phys. Oceanogr.* **42**, 2185–2205 (2012).

68. Renault, L., Masson, S., Arsouze, T., Madec, G. & McWilliams, J. C. Recipes for how to force oceanic model dynamics. *J. Adv. Model. Earth Syst.* **12**, e2019MS001715 (2020).

69. Cole, S. T. et al. Ice and ocean velocity in the Arctic marginal ice zone: ice roughness and momentum transfer. *Elementa* **5**, 55 (2017).

70. Martin, T., Tsamados, M., Schroeder, D. & Feltham, D. L. The impact of variable sea ice roughness on changes in Arctic Ocean surface stress: a model study. *J. Geophys. Res. Oceans* **121**, 1931–1952 (2016).

71. Brenner, S., Rainville, L., Thomson, J., Cole, S. & Lee, C. Comparing observations and parameterizations of ice-ocean drag through an annual cycle across the Beaufort Sea. *J. Geophys. Res. Oceans* **126**, e2020JC016977 (2021).

72. Li, X. et al. Eddy activity in the Arctic Ocean projected to surge in a warming world. *Zenodo* https://doi.org/10.5281/zenodo.10020010 (2023).

73. Scholz, P. et al. FESOM/fesom2: FESOM2.0.7. *Zenodo* https://doi.org/10.5281/zenodo.4742242 (2021).

74. Jülich Supercomputing Centre. JUWELS cluster and booster: exascale pathfinder with modular supercomputing architecture at Juelich Supercomputing Centre. *J. Large Scale Res. Facil.* **7**, A183 (2021).

## Author contributions

Q.W. and T.J. conceived the study. X.L. performed the simulations and analysed the model results with the support of all coauthors. X.L. and Q.W. wrote the initial paper. All authors contributed to interpreting the results and improving the paper.

## Competing interests

The authors declare no competing interests.

## Additional information

**Extended data** is available for this paper at https://doi.org/10.1038/s41558-023-01908-w.

**Correspondence and requests for materials** should be addressed to Qiang Wang.

**Peer review information** *Nature Climate Change* thanks Carolina Dufour, Mukund Gupta and the other, anonymous, reviewer(s) for their contribution to the peer review of this work.

**Reprints and permissions information** is available at www.nature.com/reprints.
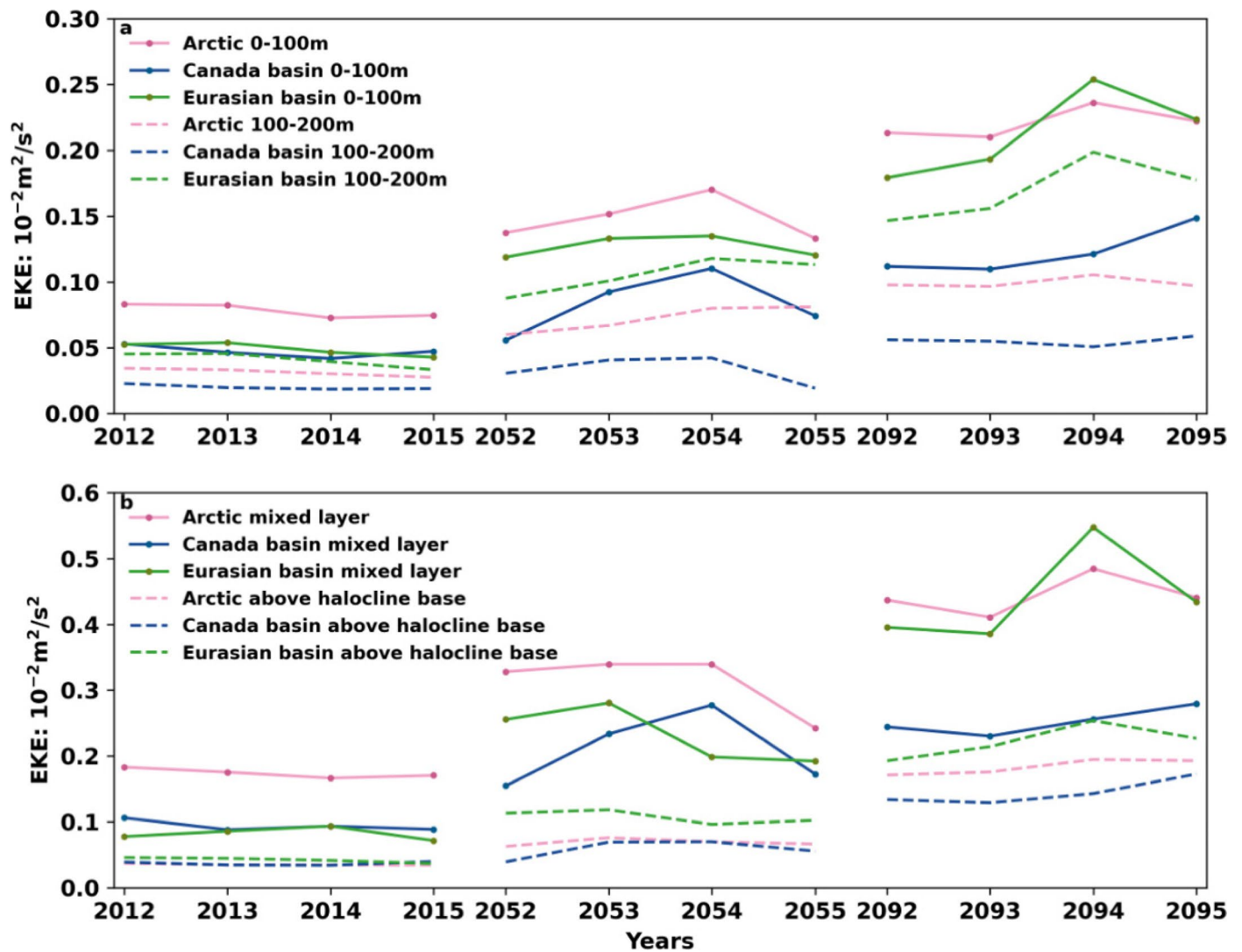
**Extended Data Fig. 1 | EKE in two depth ranges, mixed layer and above halocline base from the 1 km resolution simulations.** (a) The solid and dashed lines represent the mean EKE in the top 100 m and in the 100-200 m depth range, respectively. (b) The solid and dashed lines represent the mean EKE in the mixed layer and above halocline base depth, respectively. We compute mixed layer depth as the depth at which the potential density differs by 0.1 kg/m³ from the surface density, and halocline base depth as the depth where the ratio of temperature-induced vertical density gradient to salinity-induced vertical density gradient reaches 0.05. The pink, blue, and green lines depict the EKE of the Arctic Ocean, Canada Basin and Eurasian Basin, respectively.
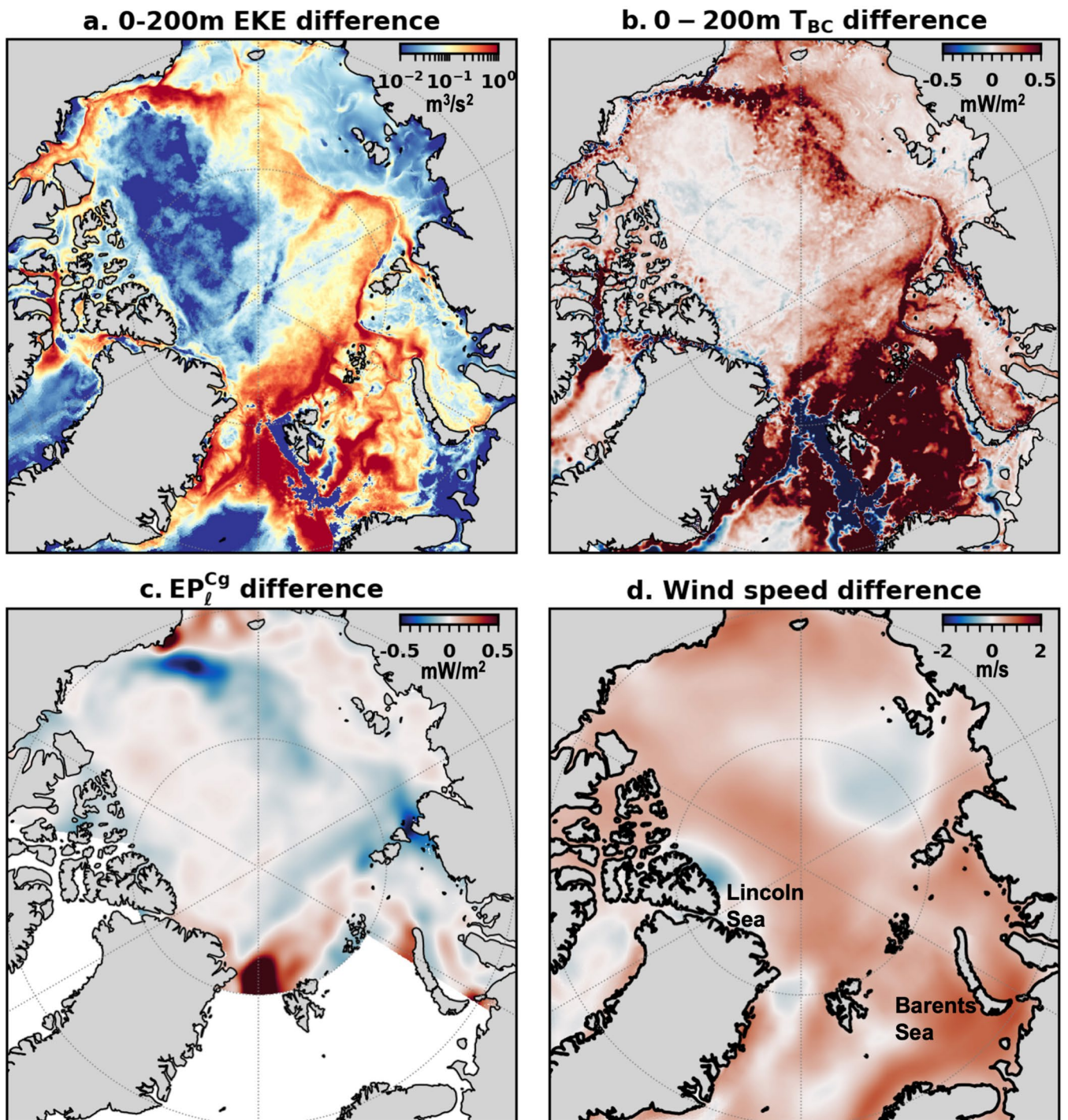
**Extended Data Fig. 2 | Difference of EKE, baroclinicity, surface power and wind speeds between 2092-2095 and 2012-2015 in eddy-rich simulations.**
The difference of (a) EKE, (b) baroclinicity, (c) surface power at 50 km spatial scale, and (d) wind speeds (2092-2095 minus 2012-2015).
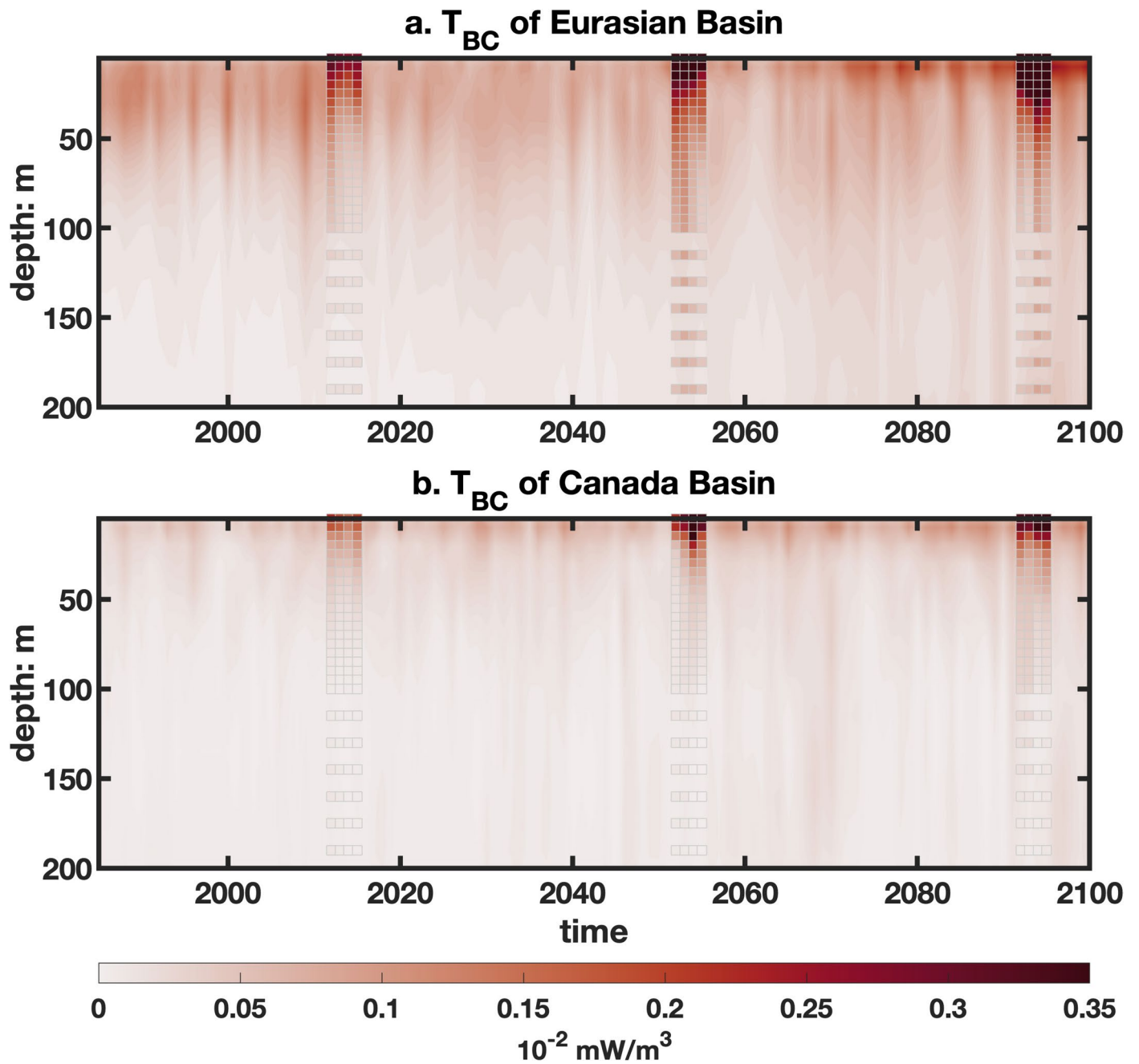
Extended Data Fig. 3 | Hovmöller diagram of baroclinicity in Eurasian basin (a) and Canada basin (b). The 4.5 km resolution simulation is shown in the background, while the 1 km resolution simulation is depicted with small squares for the three time slices.
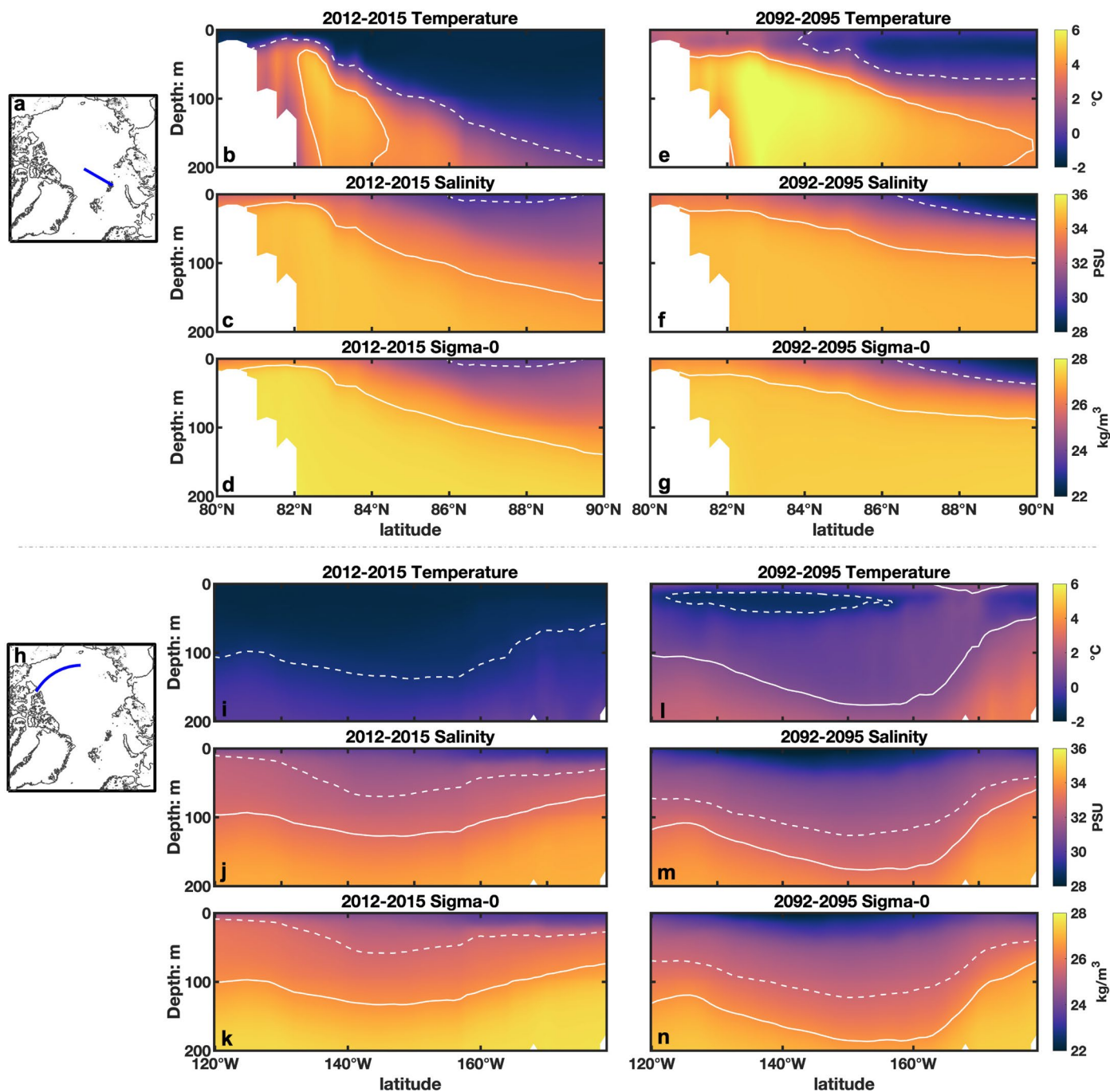
**Extended Data Fig. 4 | Temperature, salinity and sigma-0 in two transects in different climate scenarios.** (b,c,d) and (i,j,k) for 2012-2015. (e,f,g) and (l,m,n) for 2092-2095. The locations of the transects are marked by the blue lines in a and h. For the transect in panel a, the white dashed and solid lines represent the 0.5°C and 4°C isotherms in panel b,e; the 30 and 34 psu isohalines in panels c and f, and the isopycnals of 24 and 27 kg/m³ in panels d and g. The Atlantic Water boundary current is mainly located in the latitude range between 82.5°N and 85°N in this transect, where the isopycnal slope is flatter in 2092-2095. For the transect in panel h, along 75°N across the central Canada Basin, the white dashed and solid lines represent the -1°C and 1°C isotherms in panel i,l; the 32 and 33 psu isohalines in panels j and m, and the isopycnals of 25.5 and 26.5kg/m³ in panels k and n. This figure indicates that the Beaufort Gyre will accumulate more freshwater, thus possessing higher available potential energy, in the future warming climate. Sigma-0 refers to the density of water in kg/m³ when brought adiabatically to the surface, with 1000 kg/m³ subtracted.
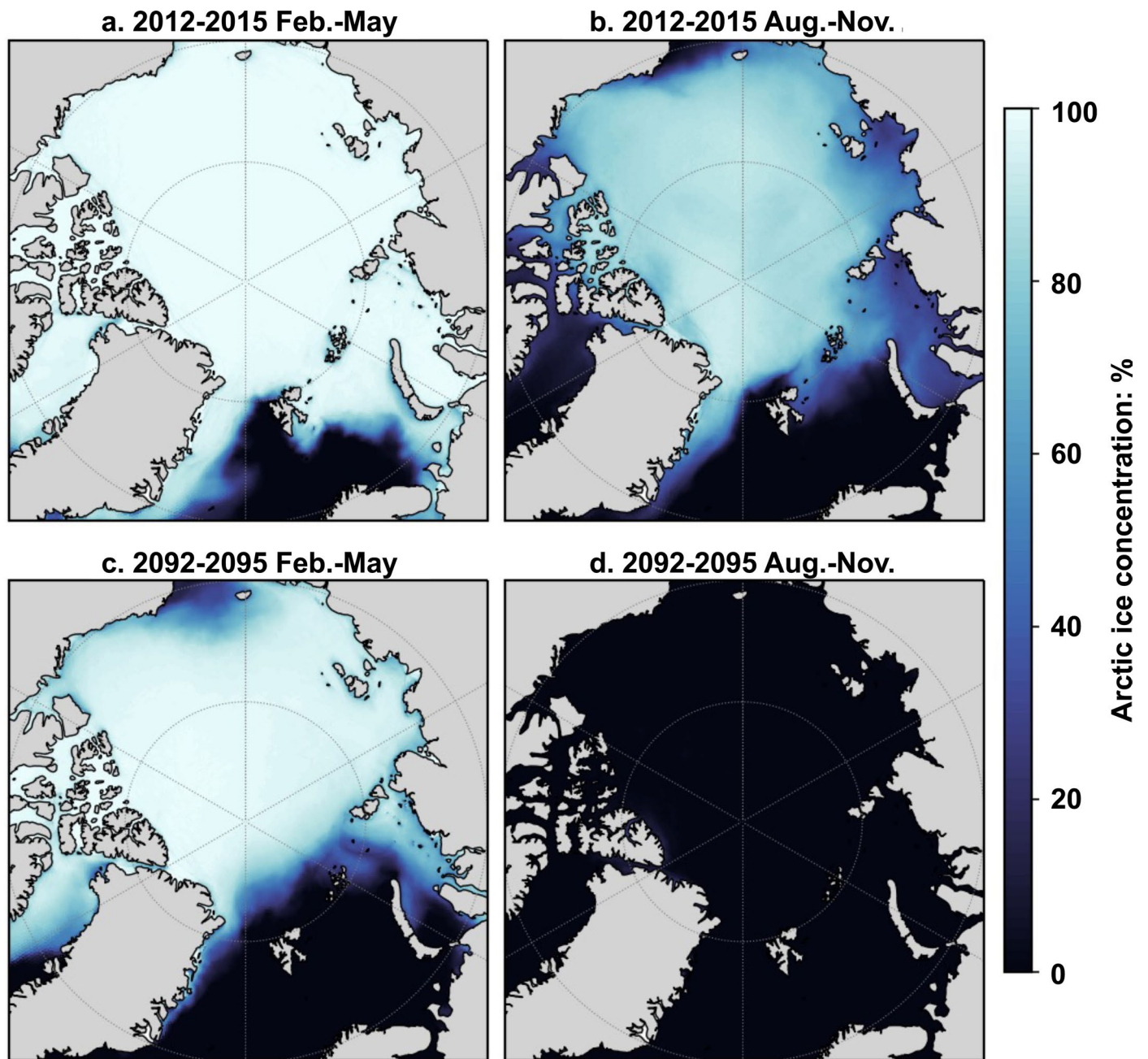
**Extended Data Fig. 5 | Arctic sea ice concentration.** a,c Mean Arctic ice concentration for February to May (Feb.-May) during (a) 2012-2015 and (c) 2092-2095. b,d Mean over August to November (Aug.-Nov.) during (b) 2012-2015 and (d) 2092-2095.
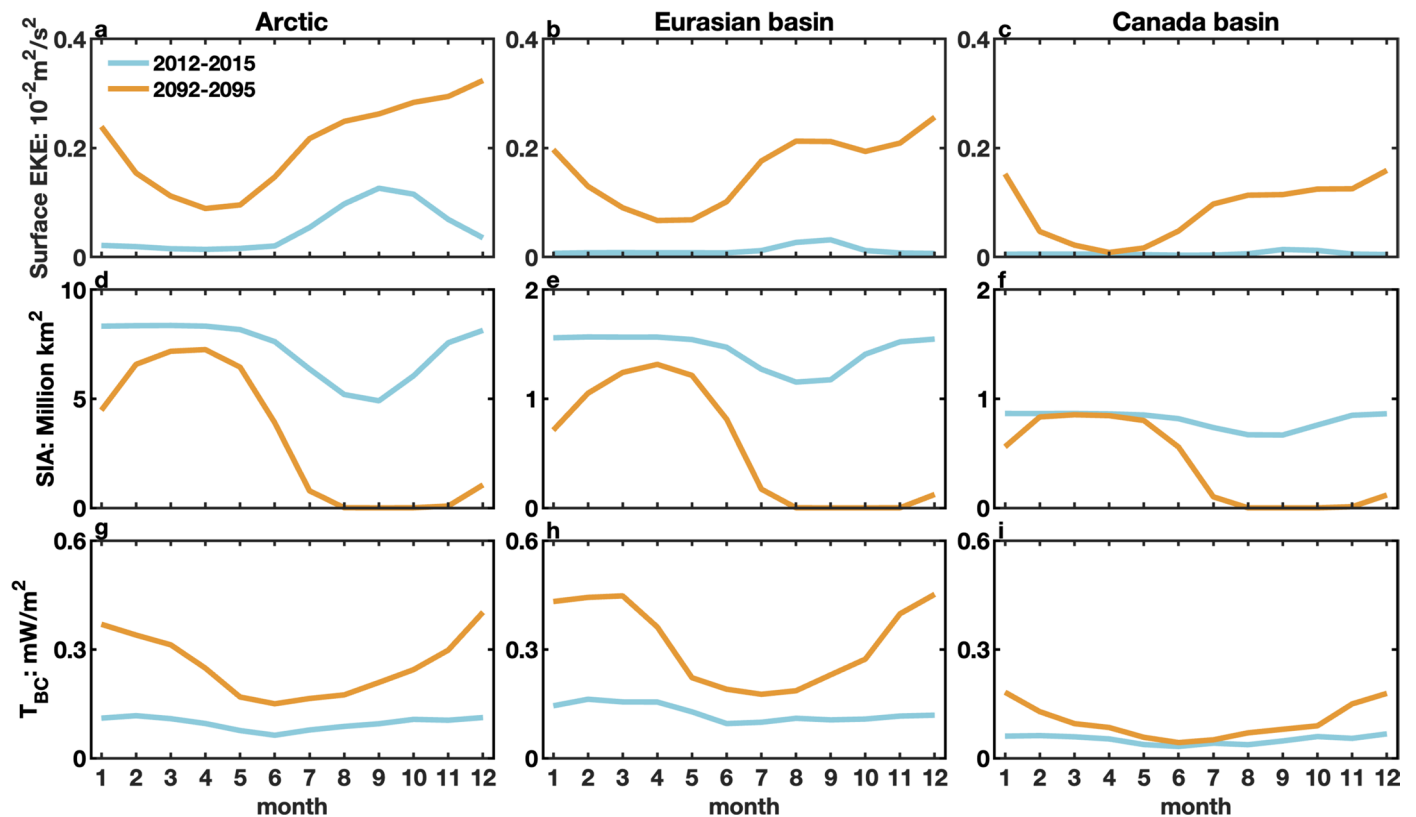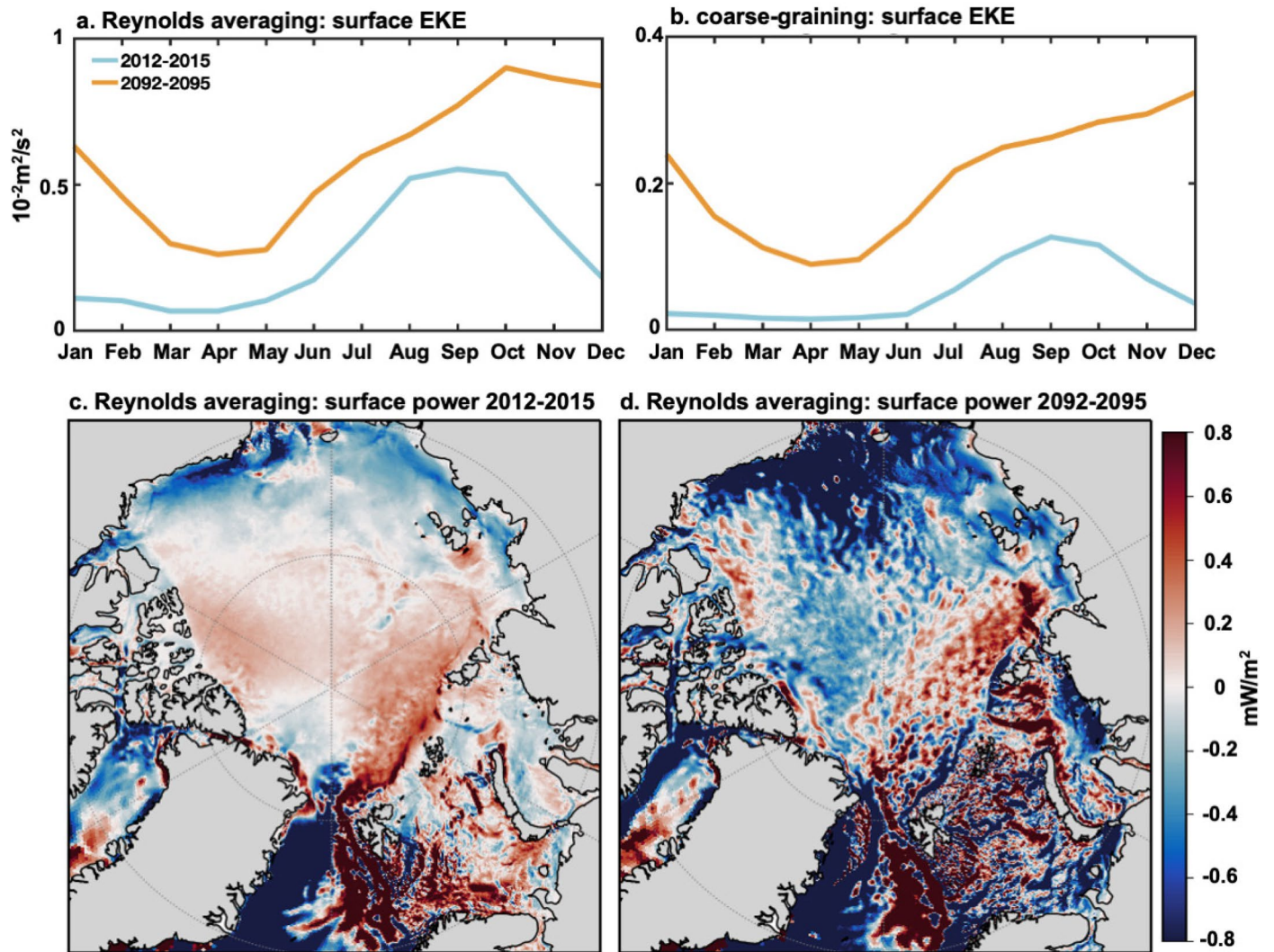
**Extended Data Fig. 6 | Seasonal cycle of ocean surface EKE, sea ice area (SIA) and baroclinicity in eddy-rich simulations.** a,b,c: Seasonal cycle of ocean surface EKE in [blue] 2012-2015 and [orange] 2092-2095 for (a) Arctic Ocean, (b) Eurasian Basin and (c) Canada Basin. d,e,f: Seasonal cycle of SIA in the two periods for (d) Arctic Ocean, (e) Eurasian Basin and (f) Canada Basin. g,h,i: Seasonal cycle of baroclinicity in the two periods for (g) Arctic Ocean, (h) Eurasian Basin and (i) Canada Basin. The correlation coefficients between ocean surface EKE and SIA are -0.92, -0.90 and -0.56 in 2012-2015 for the Arctic Ocean, Eurasian Basin and Canada Basin, respectively. They are -0.88, -0.90, -0.79 in 2092-2095. All the correlations are significant at the 95% confidence level. The significant anticorrelation between EKE and SIA indicates the direct impact of seasonal sea ice on EKE at the ocean surface. On seasonal time scales, ocean surface EKE is not correlated with baroclinicity.
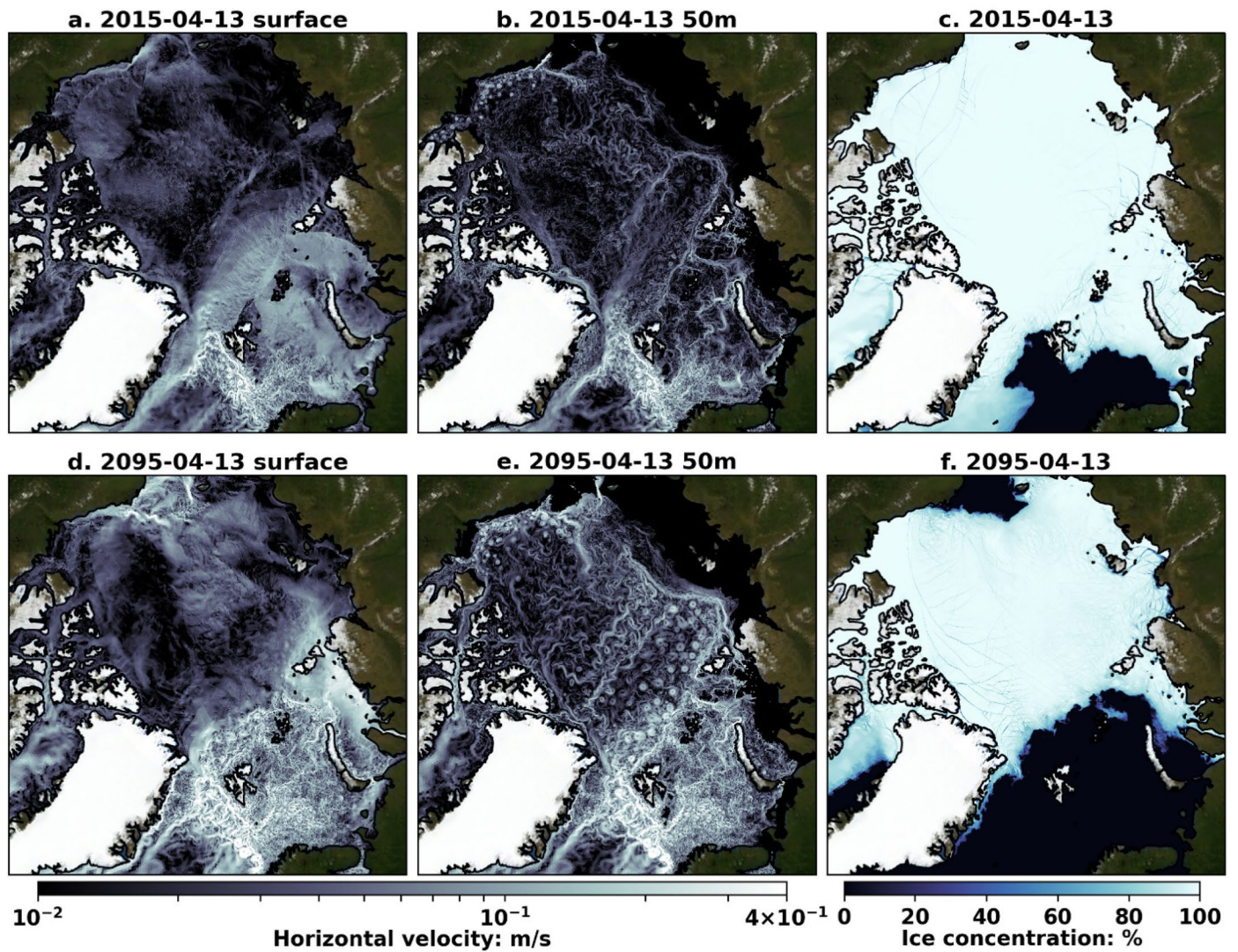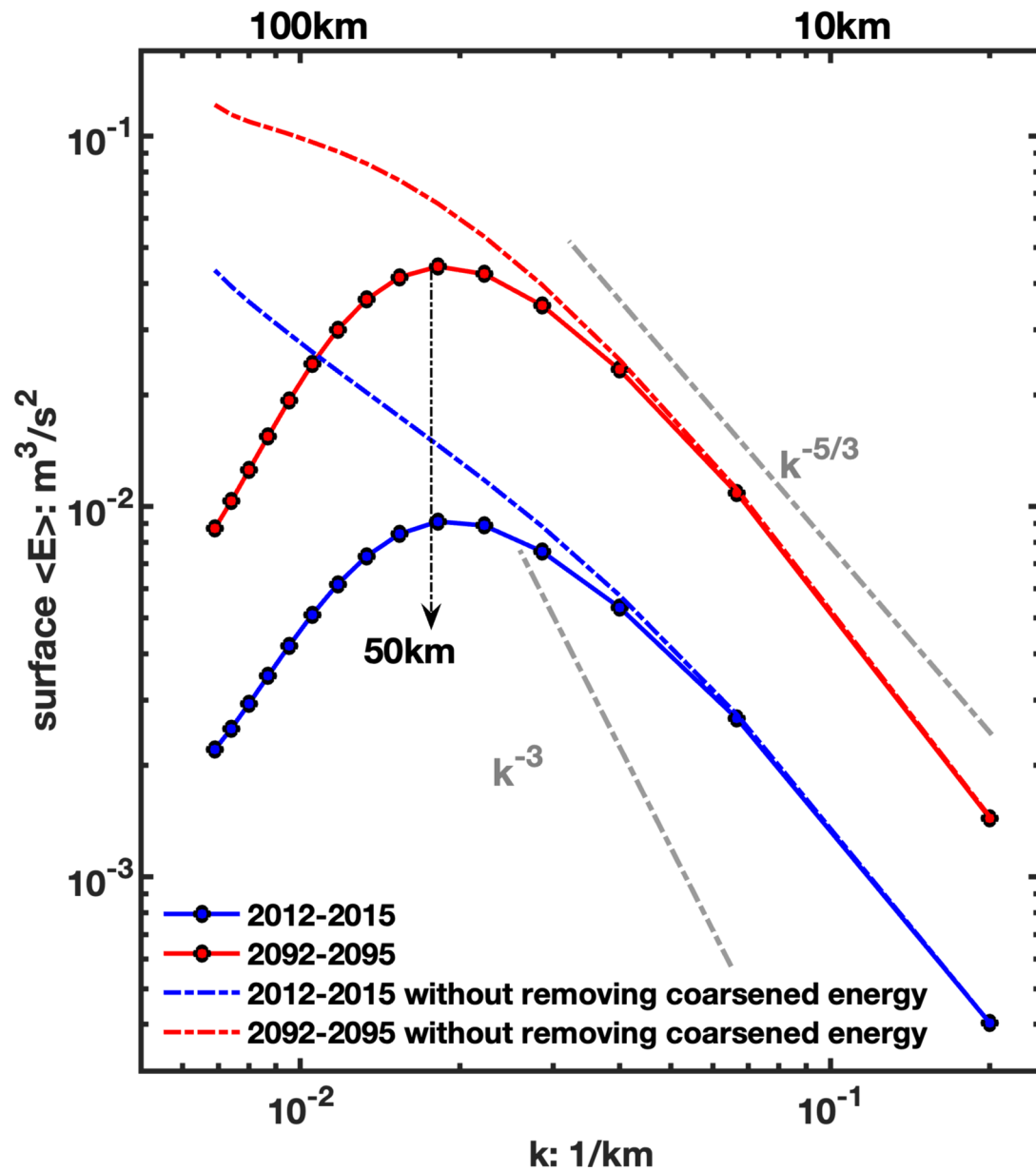
**Extended Data Fig. 7 | Arctic Ocean currents and eddy activity in different climates.** Snapshots of ocean currents and eddy activity (a,d) at surface and (b,e) 50 m depth from a FESOM simulation with 1 km resolution. The right column is the corresponding Arctic sea ice concentration (c,f). The upper row is for 13th April, 2015, and the bottom row is for the same day but in 2095. This figure indicates that eddy activity 'at ocean surface' is low in months with sea ice cover even in a warmer climate, despite that eddy activity is enhanced at depth. Credit: background image, NASA Earth Observatory.

**Extended Data Fig. 8 | Arctic Ocean surface EKE obtained from two calculation methods and surface power using the Reynolds averaging method.** Seasonal cycle of Arctic Ocean surface EKE in the two periods obtained from two calculation methods: (a) Reynolds averaging and (b) coarse-graining. Spatial pattern of surface power using the Reynolds averaging method: (c) 2012-2015 and (d) 2092-2095 periods. The definition is given in equation 3 in the Method section.

**Extended Data Fig. 9 | Energy spectrum of Arctic Ocean surface currents in two different periods of the eddy-rich simulations.** The blue lines denote the 2012-2015 period, while the red lines represent 2092-2095. Solid lines with dots show the case when energy on scales coarser than 100 km is removed before computing the spectrum; dashed lines show the case when coarse energy is not removed.
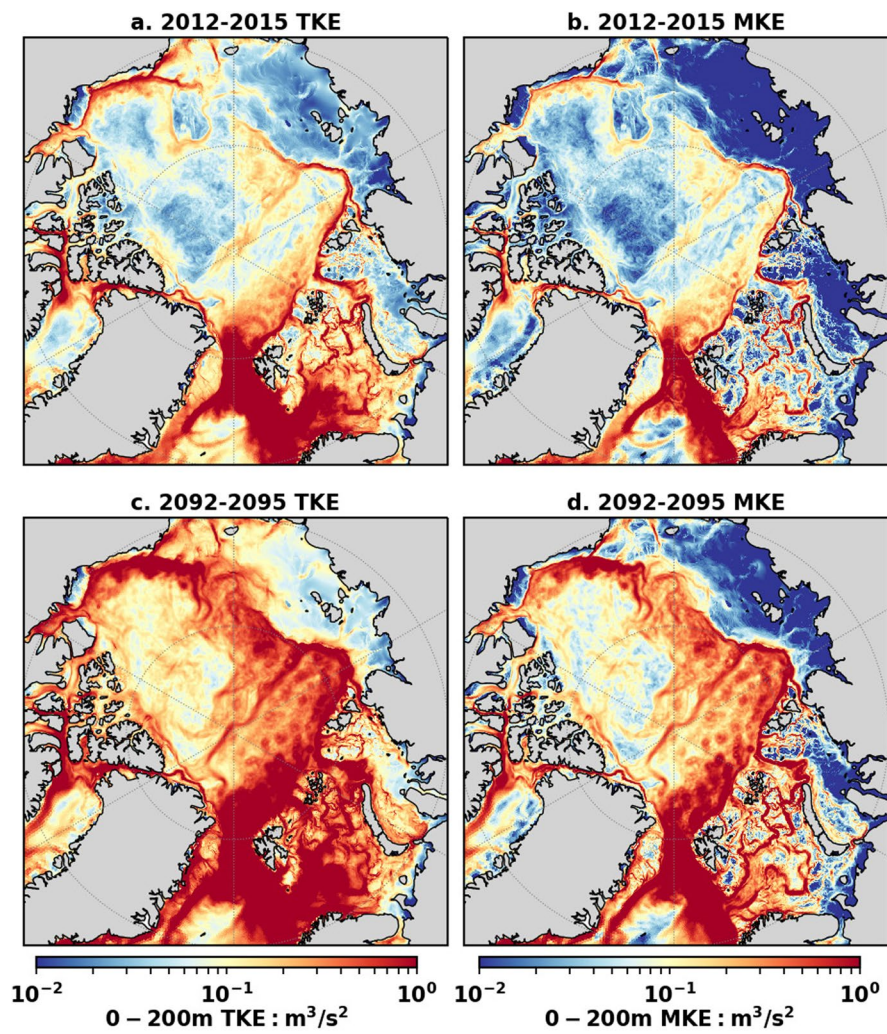
**Extended Data Fig. 10 | Total kinetic energy (TKE, left) and mean kinetic energy (MKE, right) integrated over the upper 200 meters.** a,b, for the period of 2012-2015. c,d, for the period of 2092-2095.